

Article

Real-Time Implementation and Control of Multi-Source Electric Vehicle Traction Motor under Various Drive Conditions

Achikkulath Prasanthi ¹, Hussain Shareef ^{1,2,*}, Rachid Errouissi ¹, Madathodika Asna ¹ and Addy Wahyudie ¹

¹ Department of Electrical and Communication Engineering, United Arab Emirates University, Al Ain P.O. Box 15551, United Arab Emirates; prasanthi@uaeu.ac.ae (A.P.); rachid.errouissi@uaeu.ac.ae (R.E.); asna.m@uaeu.ac.ae (M.A.); addy.w@uaeu.ac.ae (A.W.)

² Emirates Center for Mobility Research, United Arab Emirates University, Al Ain P.O. Box 15551, United Arab Emirates

* Correspondence: shareef@uaeu.ac.ae; Tel.: +971-37135390

Abstract: The hybridization of multiple energy sources is crucial for electric vehicles to deliver the same performance as modern fossil fuel-based automobiles. This paper presents a torque and speed control strategy for an electric vehicle DC traction motor by regulating the power flow from two energy sources, namely battery and supercapacitor systems, to resist unpredictable disturbances. A control system with three control loops is applied to regulate the speed of the traction motor. The outer speed control loop is a nonlinear state feedback controller with a disturbance observer, which is capable of handling non-linear systems with unpredictable disturbances. The inner voltage and current control loop are precisely tuned PI controllers. Using an adaptive energy management method that varies depending on the state of charge of the source, the total reference current needed to support the load demand is split between two sources. A laboratory prototype system model is generated, and the performance is analyzed under motoring and regenerative braking conditions. For monitoring and controlling the system, the dSPACE DS1202 real-time simulator is employed. The performance of the proposed control system is evaluated and it is found that the settling time to settle within a tolerance band of 1% is 0.75 s.

Keywords: non-linear state feedback controller; disturbance observer; real time control; speed control; torque control; hardware prototype



Citation: Prasanthi, A.; Shareef, H.; Errouissi, R.; Asna, M.; Wahyudie, A. Real-Time Implementation and Control of Multi-Source Electric Vehicle Traction Motor under Various Drive Conditions. *Energies* **2023**, *16*, 6447. <https://doi.org/10.3390/en16186447>

Academic Editors: Eric Cheng and Junfeng Liu

Received: 2 July 2023

Revised: 4 August 2023

Accepted: 10 August 2023

Published: 6 September 2023



Copyright: © 2023 by the authors. Licensee MDPI, Basel, Switzerland. This article is an open access article distributed under the terms and conditions of the Creative Commons Attribution (CC BY) license (<https://creativecommons.org/licenses/by/4.0/>).

1. Introduction

By addressing the need for increased mobility in daily life, automobiles have significantly influenced the development of modern society. The internal combustion engine revolution has made significant contributions to the automobile industry. However, significant levels of harmful emissions, such as carbon dioxide (CO₂), carbon monoxide (CO), nitrogen oxides (NO_x), unburned hydrocarbons (HCs), and others, have been contributing to air pollution, global warming, and ozone layer depletion. The use of an alternative form of transportation is a well-known remedy for these issues [1].

The choice of an electric motor for an EV is often determined by characteristics like its ease of use, toughness, starting torque, drive control, and torque response. In low-power applications, DC motors continue to be the foundation of EV traction due to their simplicity, convenience, and high authenticity [2]. The most commonly employed speed controllers for DC traction motors in the literature include proportional controllers [3], proportional integral (PI) controllers with random tuning [4], and anti-windup PI controllers [5]. In these studies, a linearized model of the DC motor is assumed, without examining the motor's braking mode. In [2], a fuzzy self-tuning strategy was used to manage the speed of a DC traction motor to evaluate the proportional, integral, and derivative gains of the proportional–integral–derivative (PID) controller. Using a self-tuning fuzzy PID controller, the armature voltage control is executed by comparing the actual speed and reference speed.

A more advanced controller based on a linear state feedback controller and state feedback observer was presented in [6] to track the speed of a DC motor. Although the results were satisfactory in comparison with those for PI and PID controllers, the non-linear behavior, plant disturbance, and sensor noise may lead to deviations in the control performance due to linearization. As a solution to this, an integral state feedback control with the Kalman filter was proposed in [7]. The Kalman filter improved the closed-loop system's transient performance. In [8], the speed of a separately excited DC motor was estimated and controlled using artificial neural networks to accomplish precise speed trajectory control, particularly when the motor and load characteristics were unknown. Speed management of a DC motor was provided in [9] and was based on a noise-reduction disturbance observer and a traditional PI controller. With this control strategy, a linear approximation of the motor dynamics was possible. In [10], the extended Kalman filter estimator and fuzzy logic controller were suggested for sensorless speed control of DC motors. For the same purpose, PI controllers and sliding-mode controllers were utilized to control the speed of a DC motor in [11]. When the settling time, peak overshoot, and steady-state error were considered, the results showed that the sliding-mode controller (SMC) performed better than the PI controller for different step changes in load torque and reference speed. The disadvantage of SMC, as mentioned in [12], is the chattering dynamics generated by discontinuous control signals, which is further aggravated by small time delays in the system. For the speed tracking control of a set of separately excited DC motors, an adaptive fuzzy sliding mode controller was suggested in [13], where a fuzzy self-learning mechanism was used to generate the parameters of sliding mode control related to the extended feedback gain and switching gain. There has been much research performed on disturbance-observer-based nonlinear control. The purpose of the disturbance observer, an inner-loop output feedback controller, is to reject external disturbances and strengthen the outer-loop baseline controller's resistance to plant uncertainties. A super-twisting sliding mode controller with a disturbance observer has been proposed as a speed controller for permanent magnet synchronous motor (PMSM)-based variable-speed drive [14]. Similarly, in reference [15], an extended state observer-based super-twisting sliding-mode controller was used to control a DC-DC buck converter to provide a variable-DC link voltage. A disturbance observer-enhanced model predictive controller for the speed regulation of PMSM was recommended in [16]. A disturbance observer was applied, along with a Jacobian linearization model of PMSM, to control the speed [17].

In addition to the use of various control methods that can be used to control traction motors, the real-time hardware implementation of a traction system with a test bench prototype is crucial. To this end, the real-time speed control of a series DC motor using a PI speed controller with an anti-windup scheme was presented in [5]. A constant DC voltage was used as the source and the system did not consider regenerative braking and neglected the non-linearity due to the magnetic saturation of the motor to design the controller. In [9], a controller based on a classical PI controller with an anti-windup scheme and noise reduction disturbance observer was implemented on the same system as that in [5]. The controller was designed using a linear model of a DC series motor considering the magnetic saturation of the motor. A bi-directional versatile buck-boost converter with a coupled inductor was designed and implemented in [18]. In this case, the current controller employed sliding-mode control, while the voltage controller used PI control. The results presented were from tests that solely involved an open-loop speed controller. In a related study, the implementation of the speed control of a DC motor was demonstrated [19] using a fuzzy logic controller with the speed error and change in speed error as inputs to the fuzzy controller. The speed controller was tested with a multifunctional data acquisition device NI USB-6812 DAQ card and MS15 DC motor control module. Similarly, in [20], a DC/DC buck converter system was applied using flatness control for bi-directional tracking control of a DC motor system. In the meantime, a cascaded fuzzy logic controller was used to generate the torque-regulating current for an EV traction system with an indirect field-oriented induction motor drive system in [21]. Here, the EV was powered by battery

units (*BUs*) directly connected to the space vector pulse width modulation inverter without considering the variation in the terminal output voltage with state of charge (SoC). The real-time simulator DS 1103 controller board was used by the researchers for the real-time monitoring and control of the traction system. All the studies discussed above did not address power regulation from multiple sources and were based on a single energy source, such as *BUs*.

Considering the real-time hardware implementation of power flow regulation from multiple energy sources, adaptive, non-linear control of a hybrid electric vehicle (HEV) with a fuel cell–*BU*–supercapacitor (SC) hybrid source was proposed in [22]. The authors adopted a rule-based energy management to regulate the power flow from three sources. The fuel cells employed DC-DC boost converters, while the *BU* and SC used DC-DC buck boost converters. To control these converters and support a constant DC bus voltage, a sliding-mode controller was employed. Control laws were implemented using microcontrollers and the system was tested on a plant model simulated on Simulink. In a related study, a multi-input converter system with two sources, namely a *BU* and SC, was recommended in [23] with rule-based energy management and a fuzzy-PI hybrid controller. The cases of regenerative braking and load torque change were not analyzed in that study. Similar to [22], a hybrid fuel cell and batteries system was suggested in [24] with a fuzzy logic-based energy-management system to generate the reference power output of the fuel cell. Meanwhile, a PI controller served as both the voltage and current controller for the *BU* to keep a constant voltage across the DC bus and as the current controller for the fuel cell. The authors used a real-time simulator OPAL-RT LAB platform. Despite using a real source and motor load, the system was coded in C language for execution. The same system with a *BU* and SC was implemented in [25] with fuzzy energy management, whose function was to produce the reference power demand of the SC. Similar to the control in [24], PI controllers were used to maintain the DC link voltage. The system was executed in real time using the OPAL-RT LAB simulator. However, the soft transition strategy was implemented by a simulated source and load system.

Dealing with nonlinearities and perturbation in the design of a closed-loop controller for a DC machine is still a significant problem, particularly when good dynamic performance is needed. According to the existing literature, diverse types of controllers are used to regulate the speed and torque of DC motors. Most DC motor control strategies assumed a linear system; thus the non-linear behavior and other uncertainties within the system have not been well investigated in the earlier works [26,27]. In addition, the switching action of DC-DC converters further contributes to the non-linear behavior and damped dynamics of the overall system. Furthermore, many factors, such as sensor noise, process noise, and model errors, may affect the dynamic transient behavior of the system [28,29]. Thus, it is significant to design the speed and torque controller of the traction motor considering non-linearity and other unpredictable disturbances in EV applications. To overcome the non-linearity issues, as well as to achieve fast dynamics and the desired output voltage, the design of an efficient controller is essential. The literature has overlooked the hardware implementation of power flow regulation from different energy sources to control traction motors in detail. Additionally, most of the research has used plant models simulated using the Simulink platform for testing the controller and energy management, while the actual system disturbances have not been accounted for.

Reference [29] focused on the simulation of the speed control of a DC motor with a non-linear state feedback controller (NLSFC) with a disturbance observer (DO). This paper focuses on the development of a hardware prototype that can be used as a laboratory-scale prototype. The real-time simulator dSPACE DS1202 microLabBox is used for the monitoring and control of the proposed EV DC traction motor loaded with a magnetic brake system. In addition, each element used in the experiment with the real-time dSpace1202 controller and method to extract variables for developing the control system and energy management are described in depth. With the design of the controller and development of a laboratory-scale prototype, the system can be reproduced to any rating with ease.

The main aim of this research is to implement the NLSFC with a DO speed controller for DC traction motor control using the dSPACE DS1202 microLabBox control desk. Considering the above discussion, the following contributions are made in this paper.

1. The hardware of DC traction motor control from two energy sources using the NLSFC with DO is implemented in real time;
2. An adaptive energy management strategy is adopted to regulate the power flow from two energy sources;
3. The developed system is tested with a laboratory prototype for varying speed references and load torque conditions, including the regenerative braking mode.

The rest of this paper is structured as follows. The overall system description is explained in Section 2. In Section 3, we introduce the controller modeling in Simulink and its interface to the real-time system, where the converter, converter controller, and speed controller design is explained in detail. Section 4 presents the energy management implementation. The equipment used for the hardware is explained in Section 5. Section 6 discusses the experimental results with three case studies and, finally, conclusions are presented in Section 7.

2. System Description

The overall system demonstration is shown in Figure 1. Two Chroma 62060D-600 programmable DC power supplies are used in place of *BUs* and an SC. Power electronic converters that act as H-bridge converters and can run in both the boost and buck modes are connected to both energy sources. A multi-function IGBT converter module with a built-in isolated IGBT driver (SEMITEACH IGBT) is applied as the H-bridge converter. The output ports of these two converters are connected to a common DC bus capacitor in parallel and function as a controlled DC input to the traction motor. The DC traction motor's shaft is joined to a speed sensor E40H12-2000-3-V-24 for sensing the speed output of the motor. To vary the motor input load torque, an MBL/MBZ brake along with a controller is utilized as a braking system in this study. The traction motor used is a separately excited DC motor. For field excitation, the field winding of the motor is connected to a Chroma 62000H programmable DC power supply. The current and voltage at different regions of the overall system are sensed using an isolated voltage and current sensor module (USM-31V). The speed sensor output (digital) and voltage–current sensor output (analog) are given as inputs to the real-time simulator DS1202. Based on the input signals and model implemented using the Simulink interface, gate pulses are generated, which control the switches in the power electronic converters via a level shifter to match the IGBT driver circuit supply voltage. This physical system is then linked to the Simulink control models via DS 1202.

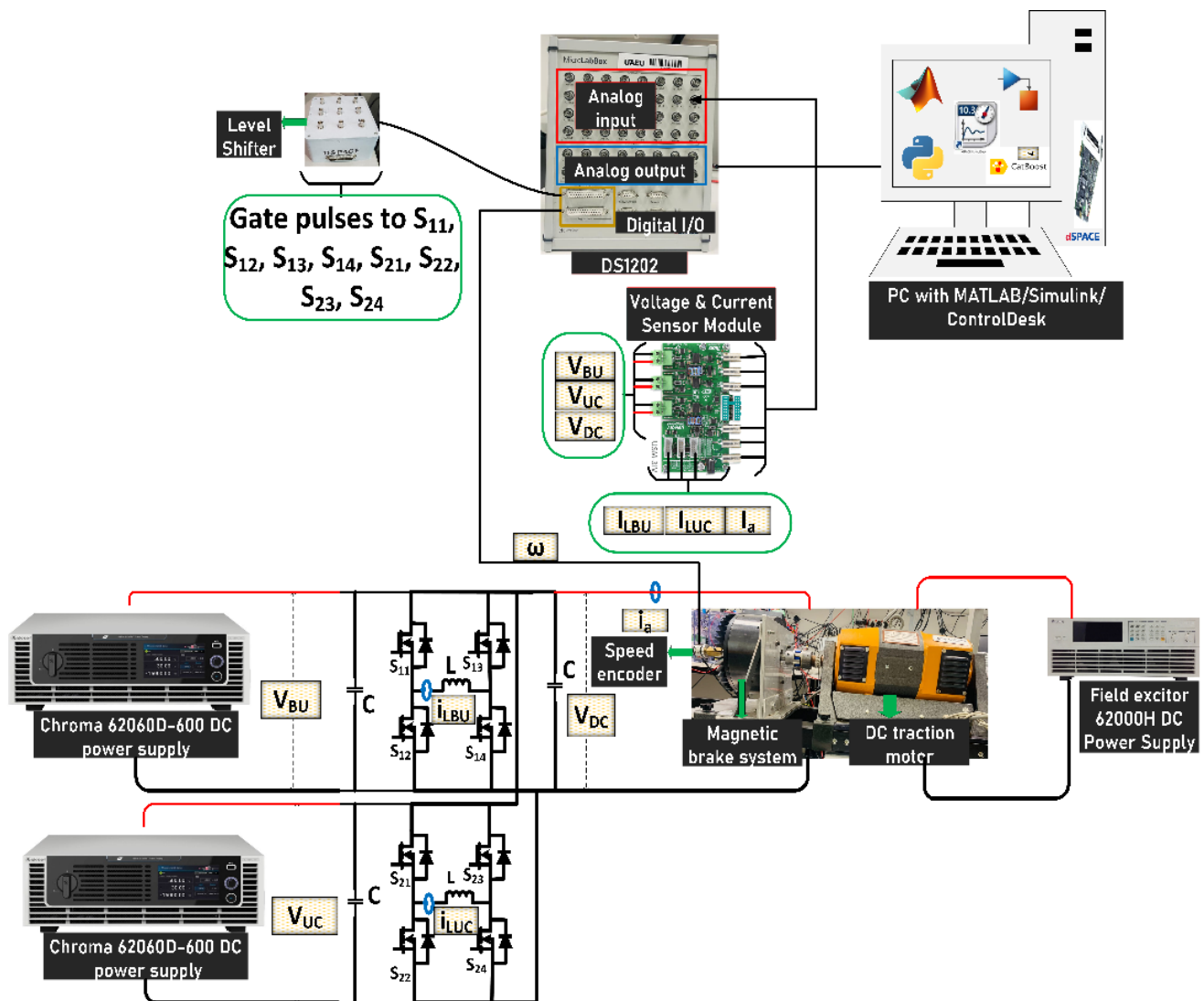


Figure 1. Demonstration of speed control of traction motor with multiple energy sources.

3. Controller Modeling in Simulink and Its Interface with the Real-Time System

The DS1202 controller board performs some actions to produce the digital control signals during each discrete time step. With the aid of the MATLAB/Simulink real-time interface, the type of action is determined by the programmed code implemented in the controller board. Using input/output (I/O) channels, the DS1202 board keeps track of the input (such as motor current, speed, voltage, etc.) for each discrete time step. The programmed action is used to generate the regulated digital signals based on the inputs and the variables that need to be controlled, such as motor speed or torque. The DS1202 controller board reads the motor current, DC voltage, source voltage, source current, and speed output from the encoder from the experimental setup through the I/O channels.

The general schematic of the control system with energy management for the proposed system is shown in Figure 2. As shown in Figure 2, the reference speed (ω_{ref}) is compared with the actual speed (ω) to generate the error in speed ($\Delta\omega$). This is given as the input to the proposed speed controller, that is, NLSFC with DO. The output of the speed controller (V_{DC_ref}) is the armature voltage needed to support the required speed and load torque at the traction motor, and this should be equal to the voltage produced at the DC link. The V_{DC_ref} generated by the speed controller is correlated with the actual voltage at the DC bus capacitor (V_{DC}) to produce the error in the DC link voltage (ΔV_{DC}). The ΔV_{DC} acts as an input to the voltage PI controller to generate the required reference source current

(I_{ref}). As the proposed system consists of two sources, the I_{ref} needs to be split among two sources (I_{1_ref} and I_{2_ref}) using energy management. Here, the energy management outputs the power split ratio (PSR) of BU (PS_1), which, when multiplied with I_{ref} to obtain I_{1_ref} and when subtracted from the total reference source current, gives I_{2_ref} . The BU and SC current PI controller compares the respective reference source current with the output source current and produces the duty pulse required for switching the respective converters. The following subsection provides a detailed explanation of the converter’s specifics, switching, speed controller design, and converter controller design.

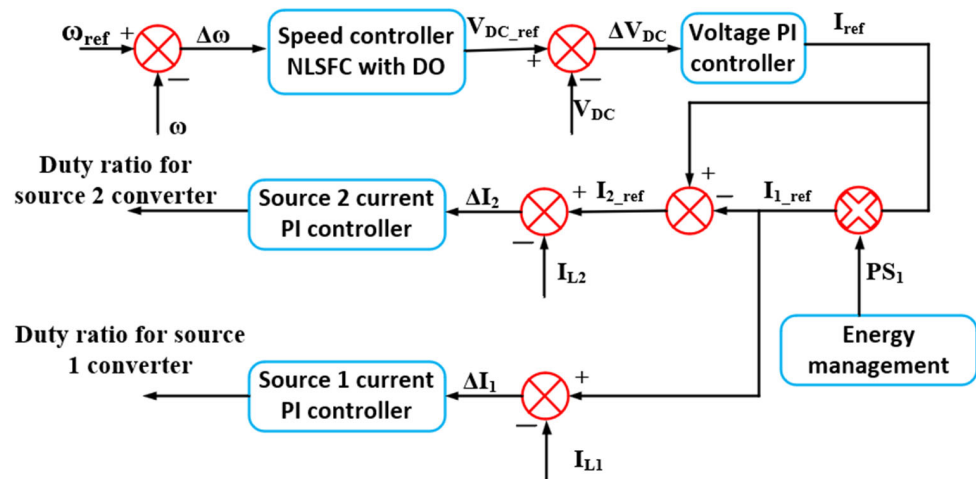


Figure 2. Schematic diagram of controller and energy management.

3.1. Converter Topology

Considering the dynamic variation in the actual energy sources used (BU and SC) in EV, a bi-directional H bridge converter is adopted in this work. This converter can step up (boost) and step down (buck) the voltage in both directions. The H bridge converter is shown in Figure 3.

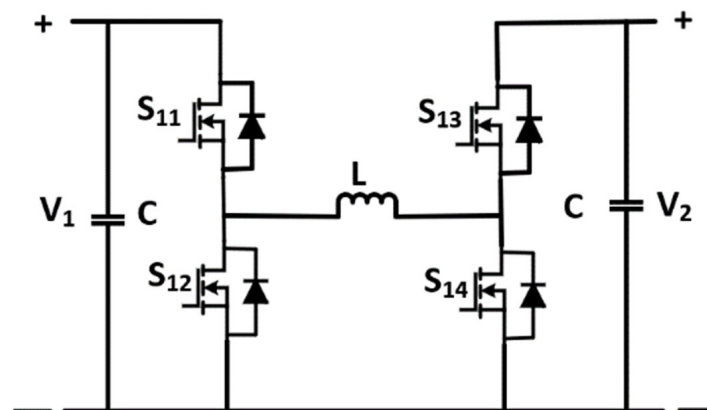


Figure 3. Bi-directional H-bridge DC-DC converter.

The various switching modes for forward boosting, forward bucking, reverse boosting, and reverse bucking are shown in Table 1. For instance, in the forward boost mode, S_{11} and S_{12} are always ON and OFF, respectively, while S_{13} and S_{14} have controlled operation regulated by the duty ratio generated by the controller and these pulses are complementary.

Table 1. Modes of operation of switches in the H bridge converter.

| Operation Mode | S ₁₁ | S ₁₂ | S ₁₃ | S ₁₄ |
|----------------|-----------------|-----------------|-----------------|-----------------|
| Forward boost | ON | OFF | Controlled | Controlled |
| Forward buck | Controlled | Controlled | ON | OFF |
| Reverse boost | Controlled | Controlled | ON | OFF |
| Reverse buck | ON | OFF | Controlled | Controlled |

3.2. Converter Controller

The control block diagram of the H bridge converter controller is represented in Figure 4. As explained before, in this work, the voltage and current controller used are PI controllers. In Figure 4, K_{pv} and K_{iv} are the proportional and integral gains of the PI voltage loop control, respectively. K_{pi} and K_{ii} represent the proportional and integral gains of the current loop control, respectively. D_{buck} is the duty ratio when the converter is operating in buck mode and D_{boost} is the duty ratio when the converter is working in boost mode. The closed loop outer-voltage-control closed loop transfer function can be expressed as [29]:

$$\frac{V_{DC}}{V_{DC_ref}} = \left(\frac{sK_{pv}}{C} + \frac{K_{iv}}{C} \right) / \left(s^2 + \frac{sK_{pv}}{C} + \frac{K_{iv}}{C} \right) \tag{1}$$

where L and C are the inductor and capacitor values present in the H bridge converter displayed in Figure 3, respectively.

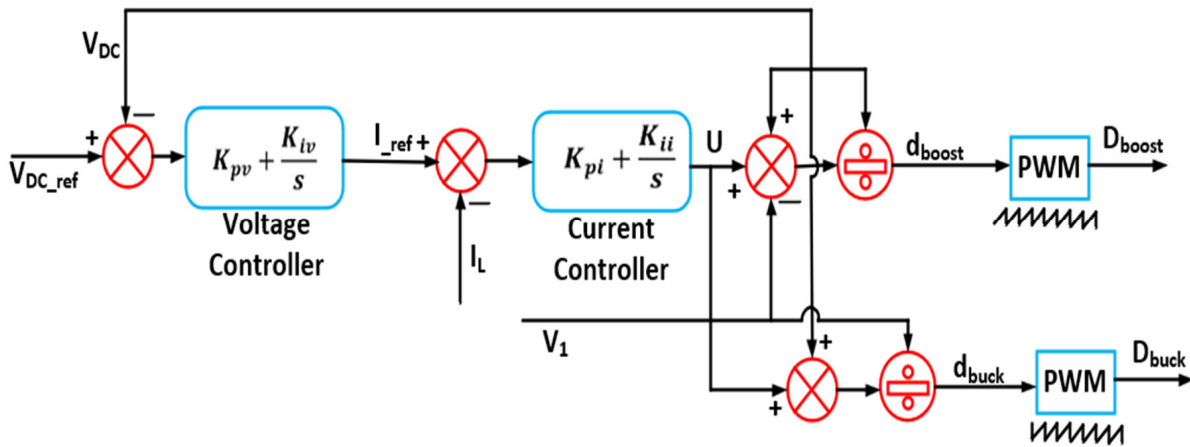


Figure 4. Block diagram of voltage and current controller for single source.

The denominator of Equation (1) can be compared with the second-order characteristic equation; thus, the PI tuning parameters can be obtained as:

$$K_{pv} = 2\xi_v\omega_v C \tag{2}$$

$$K_{iv} = C\omega_v^2 \tag{3}$$

where ξ_v is the damping ratio and ω_v is the natural frequency of oscillation of the voltage control loop. The inner current loop transfer function with U/I_L as the open loop transfer function can be expressed as [29]:

$$\frac{I_L}{I_{L_ref}} = \left(\frac{sK_{pi}}{L} + \frac{K_{ii}}{L} \right) / \left(s^2 + \frac{sK_{pi}}{L} + \frac{K_{ii}}{L} \right) \tag{4}$$

As in the voltage control loop, the denominator of Equation (4) can be correlated with the standard second-order characteristic equation; thus, K_{pi} and K_{ii} can be obtained as:

$$K_{pi} = 2\xi_i\omega_iL \tag{5}$$

$$K_{ii} = L\omega_i^2 \tag{6}$$

where ξ_i is the damping ratio and ω_i is the natural frequency of oscillation of the current control loop. The duty cycle for the boost operation can be obtained from the following relation [29],

$$d_{\text{boost}} = \frac{U - V_1}{V_{\text{DC}}} + 1 \tag{7}$$

where V_1 is the voltage output to the converter from the source, as represented in Figure 3.

Similarly, for the buck converter, the duty cycle for the buck operation can be expressed as [29]:

$$d_{\text{buck}} = \frac{U + V_{\text{DC}}}{V_1} \tag{8}$$

Figure 4 represents the closed loop voltage and current controller for one of the energy sources, with respect to Equation (7) and Equation (8) for the buck and boost converter, respectively.

3.3. Speed Controller

Following the required output speed and load torque, the speed controller is intended to produce the $V_{\text{DC_ref}}$ for the converter controller displayed in Figure 4. Mathematical analysis of this controller is important considering the non-linear behavior of the motor and other overall system disturbances. As a separately excited DC motor is used, a thorough investigation of the modeling is required for controller design. The state space representation of a DC motor can be expressed as [30]:

$$\dot{x} = ax + bu + db \tag{9}$$

$$y = cx \tag{10}$$

where $x = \begin{bmatrix} i_a \\ \omega \end{bmatrix}$, $a = \begin{bmatrix} \frac{-r_a}{L_a} & \frac{-k_b}{L_a} \\ \frac{k_t}{j} & \frac{-F}{j} \end{bmatrix}$, $b = \begin{bmatrix} \frac{1}{L_a} \\ 0 \end{bmatrix}$, $d = \begin{bmatrix} \frac{1}{L_a} & 0 \\ 0 & \frac{-1}{j} \end{bmatrix}$, $c = [0 \ 1]$, $u = [V_{\text{DC_ref}}]$, and

$b = \begin{bmatrix} b_1 \\ b_2 \end{bmatrix}$, which is the unknown disturbances effect within the traction motor system. r_a is the armature resistance, L_a is the armature inductance, k_t is the torque constant, k_b is the back emf constant, j is the moment of inertia, F is the friction coefficient, and $V_{\text{DC_ref}}$ is the armature input voltage. In this case, $u = V_{\text{DC_ref}}$ should be controlled and, as a result, the armature voltage is used to regulate the speed of the DC traction motor.

Non-linear state feedback controllers use a linearization method that is different from the usual Jacobian linearization, which entails approximating linear features over a specified operational region. Using an algebraic transformation, the non-linear feedback linearizing technique removes the system's non-linearities and makes the linearization valid over a large operational range. The non-linear state feedback controller can be defined as [29,30]:

$$u = (cab)^{-1} \left(k_0(\omega_{\text{ref}} - \omega) + k_1(\omega_{\text{ref}} - cax - cdb) + (\omega_{\text{ref}} - ca^2x - cadb) \right) \tag{11}$$

where k_0 and k_1 are the controller tuning parameters that can be defined as the damping ratio (ξ_0) and natural frequency of oscillation (ω_0) of the closed loop speed controller, respectively. These parameters can be evaluated using the expression:

$$k_0 = \omega_0^2 \quad (12)$$

$$k_1 = 2\xi_0\omega_0 \quad (13)$$

Equation (11) can be re-arranged as:

$$u = (cab)^{-1}(k_0(\omega_{\text{ref}} - \omega) + k_1(\omega_{\text{ref}} - ca\dot{x}) + (\omega_{\text{ref}} - ca^2x) - \Delta) \quad (14)$$

where

$$\Delta = (k_1c + ca)db \quad (15)$$

Δ is considered as disturbance, and the disturbance observer within the controller enables the estimation of Δ and can be expressed as [29]:

$$\Delta = -\mu \left(\int_0^t k_0(\omega_{\text{ref}}(\tau) - \omega(\tau))d\tau + k_1(\omega_{\text{ref}} - \omega) + \omega_{\text{ref}} - ca\dot{x} \right) \quad (16)$$

where μ is a constant value greater than zero.

The combination of the feedback controller in Equation (14) and disturbance observer in Equation (16) provides the expression for a non-linear state feedback controller with disturbance observer for the DC traction motor and is represented as:

$$u = M \left(K_I \int_0^t (\omega_{\text{ref}}(\tau) - \omega(\tau))d\tau + K_P(\omega_{\text{ref}} - \omega) + K_Y(\omega_{\text{ref}} - ca\dot{x}) + (\omega_{\text{ref}} - ca^2x) \right) \quad (17)$$

where,

$$M = (cab)^{-1} \quad (18)$$

$$K_I = \mu k_0 \quad (19)$$

$$K_P = k_0 + \mu k_1 \quad (20)$$

$$K_Y = k_1 + \mu \quad (21)$$

The schematic block diagram representation of the speed controller is shown in Figure 5. This is the block diagram implementation of Equation (17).

3.4. Implementation of Controller in Simulink

With the use of Simulink, one can create model-based designs, such as control system designs. From within the Simulink library browser, it is possible to access the DS1202's I/O ports. Once a control system has been created in Simulink, it can be built using the real-time possibility (by pressing CTRL + B), which implements the entire system inside the DSP of the DS1202 board. In this way, the control system that was previously in the software (Simulink- MATLAB R2020a) becomes a real-time system on hardware.

After building the control system, Simulink creates an *.sdf file. This file grants control-system variables, such as reference speed, gain, tuning the controller, etc., to a separate software called control-desk. With the help of control-desk software, a control panel may be built that can change the control system's variables in real time while interacting with the DS1202.

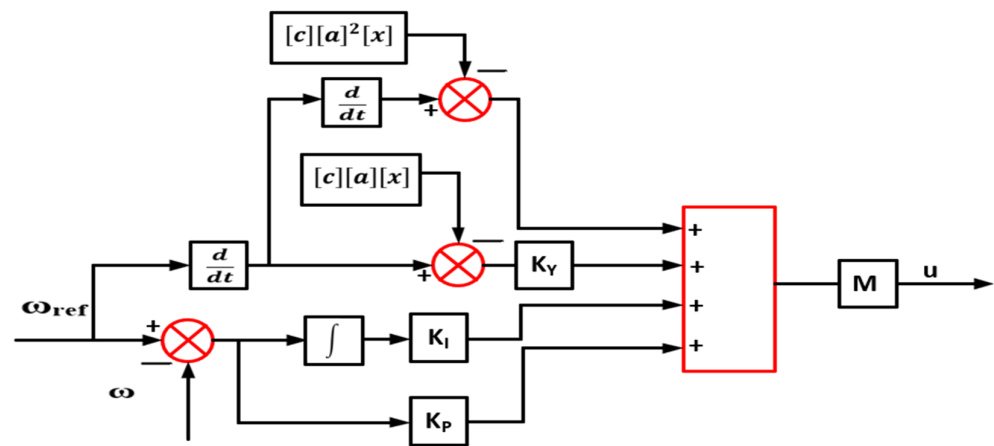


Figure 5. Schematic of speed controller.

4. Energy Management Implementation in Simulink

The energy management strategy (EMS) utilized in this study is based on dynamic source characteristics and the optimum efficiency operation zone of energy sources (*BU* and *SC*), and is adapted from [31] with minor adjustments. The total power at the motor side is to be satisfied by the *BU* and *SC*. Since *SCs* are recognized for having high operational dynamics, the *SC* is designed to take advantage of both peak and instantaneous power needs. The internal resistance of the *BU* and *SC* changes with *SoC*. The internal resistance of the *BU* will be lower at higher *SoC*, allowing the sources to produce more power. Moreover, the internal resistance of the *SC* is much lower than that of the *BU*. In this research, internal resistance characteristics are used to create a dynamic EMS.

In this EMS, a value for power demand known as P_{bound} is decided initially. Only the instantaneous power demand needs to be met by the *SC* under this threshold, and the rest of the power requirement is met by *BU*. Above the P_{bound} value, most of the power demand is satisfied by *SC*. Therefore, EMS correlates the power demand at the traction motor (P_{motor}) and the threshold P_{bound} value, and then the mode of operation is selected.

Mode 1 operation: Motoring and $P_{motor} > P_{bound}$

Then,

$$P_{UC}(t) = \frac{R_{BU}(t)}{R_{BU}(t) + R_{uc}(t)} (P_{motor}(t) - P_{bound}) \tag{22}$$

$$P_{BU}(t) = P_{motor}(t) - P_{source2}(t) \tag{23}$$

where P_{BU} and P_{SC} are the power demanded from the *BU* and *SC*, respectively. $R_{BU}(t)$ is the dynamic resistance of the *BU* and $R_{sc}(t)$ is the dynamic resistance of *SC*. When both sources are completely charged, the dynamic resistance of the *BU* will be greater than the dynamic resistance of the *SC*. As a result, as shown in Equation (22), the *SC* supplies the majority of the power over P_{bound} . This is in accordance with the *SC's* ability to meet peak power demands.

Mode 2 operation: Motoring and $P_{motor} \leq P_{bound}$

The change in power demand during a certain time is estimated using the equation:

$$\Delta P_{motor}(t) = P_{motor}(t) - P_{motor}(t - 1) \tag{24}$$

Then, the power demand from *BU* and *SC* is evaluated using the expression:

$$P_{SC}(t) = \frac{R_{BU}(t)}{R_{BU}(t) + R_{sc}(t)} \Delta P_{motor}(t) \tag{25}$$

The power requested from the *BU* is the same as that in Equation (23). Equation (25) is consistent with the features of an *SC*, which is known to meet instantaneous power demand.

Mode 3 operation: Regenerative braking

In this case, as *SC* is more effective for recovering sudden braking energy, the expression of power demanded from *SC* can be provided as:

$$P_{SC}(t) = \frac{R_{BU}(t)}{R_{BU}(t) + R_{sc}(t)} P_{motor}(t) \quad (26)$$

Then, the remaining power demand is satisfied by the *BU*, as depicted in Equation (23).

For each instance, the ratio of power output from the *BU*, which is defined as the power split ratio of the *BU*, can be defined as:

$$PSR_{BU}(t) = \frac{P_{BU}(t)}{P_{motor}(t)} \quad (27)$$

5. Equipment Used

Each component used for the experiment with the method to extract variables for building the control system and energy management using the real-time controller dSpace1202 is explained in this section.

5.1. Current and Voltage Sensor

A USM-31V fully isolated, universally connected, high-bandwidth sensor module with 3 voltage and 3 current channels was used for current and voltage measurement in the EV traction motor prototype implementation. With a $10\times/100\times/1000\times$ adjustable range for measuring the voltage and current, it can measure up to 1000 V at 100 kHz and 100 A at 200 kHz. The isolated voltage and current sensor module can be connected to controllers and monitoring equipment concurrently via multiple unipolar and bipolar output connectors, dropping the need for separate probes and many feedback sensors. The analog voltage and current outputs from this sensor module are given as analog inputs to the real-time simulator DS1202. The I/O ports of DS1202 are accessible via the Simulink library browser. Figures 6 and 7 illustrate how to create a program in Simulink to use the I/O port of DS1202 to measure the current and voltage, respectively. The ADC block in Simulink converts the analog input to a digital signal, which may then be sent as a reference input to the controller that has been programmed in Simulink for real-time operation.

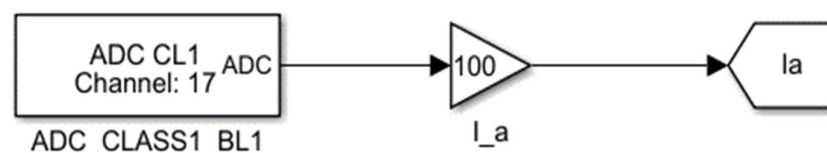


Figure 6. Real-time Simulink model for measuring armature current.

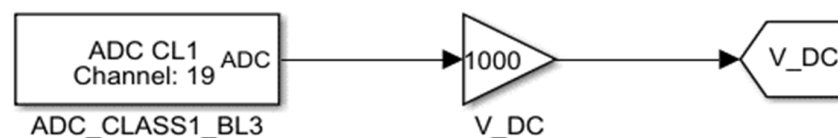


Figure 7. Real-time Simulink model for measuring DC link voltage.

5.2. DC Traction Motor with the Magnetic Brake System and Rotary Encoder

A separately excited DC motor model MV 1042–2252 kW motor with a DC excitation of 220 V and rated rotor voltage of 220 V is adopted in this work as a traction motor. The controlled voltage output of the armature is fed to the DC motor armature winding. The

DC power supply model 62000H, which has a voltage range of 0–1000 V and a current range of 0–375 A, supplies constant separate field excitation.

In addition, the magnetic braking system from the MBZ series is used to provide the motor with load torque. The torque output of the MBZ series brakes is linearly and proportionally correlated with the input voltage applied to the interface circuit. Therefore, a DC voltage signal controls the torque of the brake. The DC voltage input can vary from 0–5 V, which can be provided by the real-time simulator DS 1202, as depicted in Figure 8. The gain added to the Simulink model is based on the characteristics of DS1202. The voltage level input is accepted as a digital signal and it is converted to analog by DS1202 and fed to the brake controller through analog output channel 1.

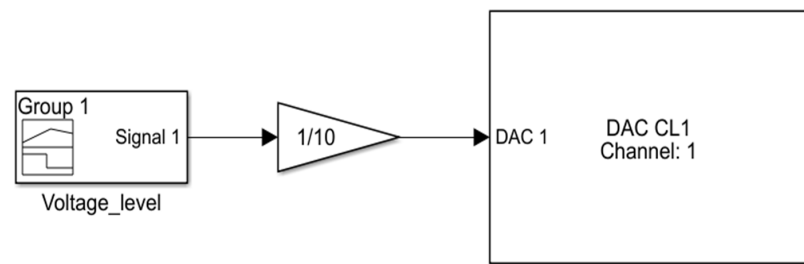


Figure 8. Real-time Simulink model supplying variable voltage to the torque controller.

The rotary encoder E40H12-2000-3-V-24 is also used in this work to measure the output speed of the motor. Owing to its wide range of mechanical and electrical applications, superior sensing, and capacity to convert mechanical movement to electric impulses, it is used in a wide variety of applications. The output type, the number of pulses per revolution, the power source, and the shape of the output signal can all be used to categorize rotary encoders into diverse groups. The I E40H12-2000-3-V-24 specifications are as follows: shaft diameter of 12 mm, 2000 pulses per revolution, signal output types of A, B, and Z, and 12–24 V power supply.

A parameter related to encoders is the number of pulses per revolution (PPR). It measures the number of pulses sent through the encoder during one full rotation, or 360 degrees, of the encoder. As the encoder rotates, the Z output type pulses once. The encoder disc crosses the preset zero location inside the encoder at that point and the signal is used to signify that. The encoder’s Z pulse output is sent as a digital input to DS1202. The DIO PWM2D Simulink block can measure the frequency and duty cycle of the input signal. The frequency is measured, and the output speed in rpm is obtained by multiplying it by 60. By taking the average of 10 samples at a sampling frequency of 10 kHz, the output speed is filtered as depicted in Figure 9.

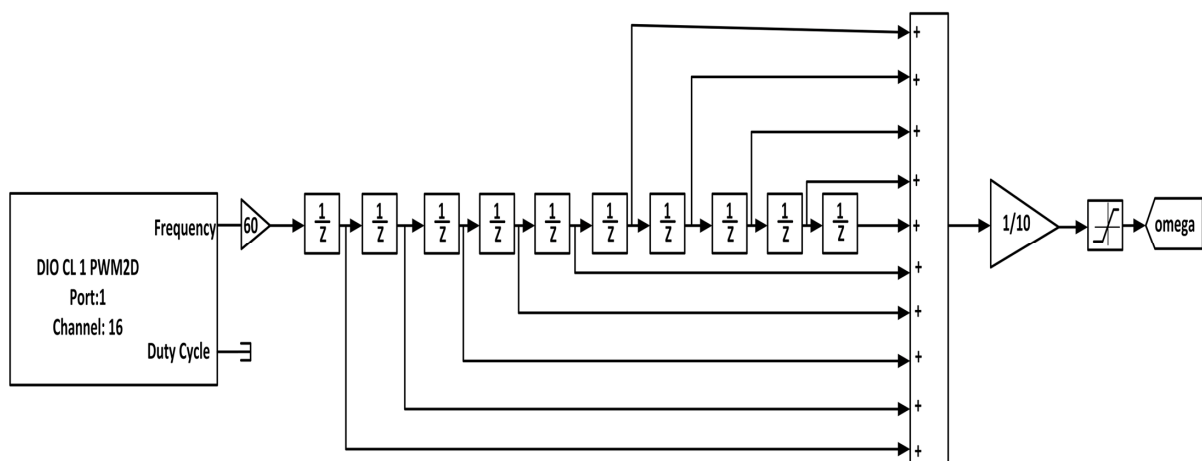


Figure 9. Real-time Simulink model for measuring speed output.

5.3. Power Electronic Converter

The SEMITEACH-IGBT module stack is used to act as a bidirectional H bridge DC converter. This is a multi-function IGBT converter with a transparent enclosure to enable internal part visibility. Both an IGBT driver and IGBT protection are built in. The module allows a maximum output and input current of 30 A, maximum input voltage of 400 V, maximum DC bus voltage of 750 V, and maximum switching frequency of 50 kHz. The typical supply voltage for the driver is 15 V. Since the maximum output voltage from DS1202 is 10 V, a level shifter is used to increase the level of the output pulse from DS1202 before providing it to the converter switches. The overall experimental setup is shown in Figure 10, with the equipment labeled.

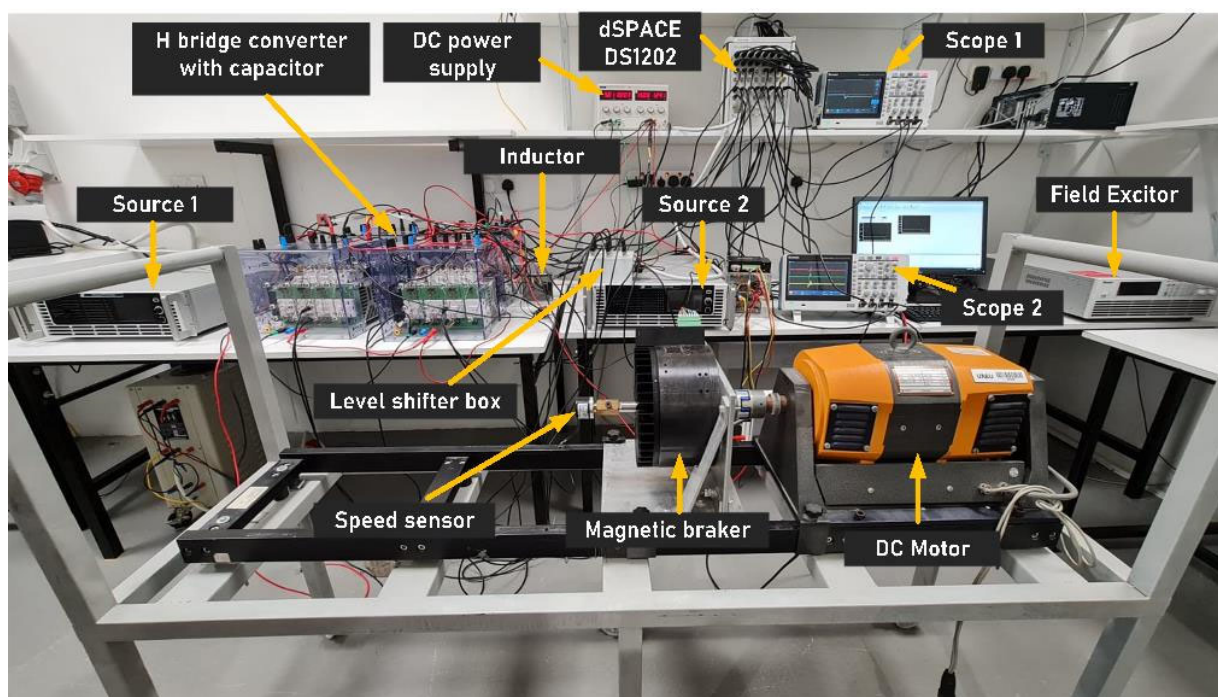


Figure 10. Experimental setup.

6. Experimental Results and Discussion

The experimental findings are presented in this section to judge how well the proposed controller performed in EV DC motor control, both experimentally and in simulation. Distinct case studies are conducted to prove the effectiveness of the system prototype. The parameters for the different controllers used for controller design along with DC motor specifications are presented in Table 2.

Table 2. DC motor specification and controller parameters used for experimentation.

| Parameter | Value |
|---|----------|
| Armature resistance, r_a (Ω) | 3.9 |
| Armature inductance, L_a (H) | 0.010879 |
| Moment of inertia, J ($\text{kg}\cdot\text{m}^2$) | 0.18 |
| Torque constant, k_t ($\text{N}\cdot\text{m}/\text{A}$) | 1.221 |
| Back emf constant, k_b ($\text{V}/(\text{rad}/\text{s})$) | 1.40 |
| Rated voltage (V) | 220 |
| Field voltage (V) | 220 |

Table 2. Cont.

| Parameter | Value |
|---|-----------|
| Damping ratio of outer voltage loop, ξ_v | 0.707 |
| Natural frequency of oscillation of voltage loop, ω_v (rad/s) | 500 |
| Damping ratio of the inner current loop, ξ_i | 0.707 |
| Natural frequency of oscillation of current loop, ω_i (rad/s) | 100 |
| Switching frequency, f_{sw} (Hz) | 10,000 |
| Sampling frequency (Hz) | 1,000,000 |
| Damping ratio of the speed control loop, ξ_0 (rad/s) | 0.707 |
| Natural frequency of oscillation of speed control loop (ω_0) (rad/s) | 20 |
| Constant, μ | 2 |

The EMS depends on the internal resistance of the BU and SC; thus, the model of these sources needs to be investigated to determine the internal resistances. For both energy sources, the second-order Thevenin model was investigated, as represented in Figure 11. R_0 is the series internal resistance of source. $R_{min}C_{min}$ denotes the parameters reflecting the source's short-term transient impacts, while $R_{sec}C_{sec}$ denotes the parameters indicating the source's long-term transient effects.

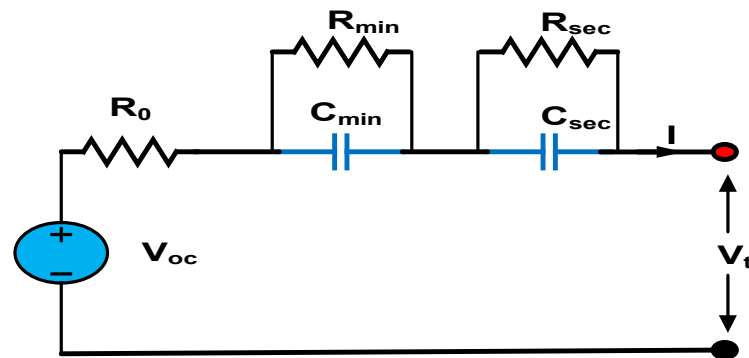


Figure 11. BU and SC model.

The dynamic variation in the BU parameters (R_{0BU} , R_{minBU} , and R_{secBU}) was adopted from the specification of Panasonic 18,650 battery cells (2.25 Ah, 3.6 V) with lithium iron phosphate (LiFePO₄) chemistry [2,31].

$$R_{0BU} = \left[0.07446 + 0.1562e^{-24.37SoC_{BU}} \right] \frac{n_{sBU}}{n_{pBU}} \quad (28)$$

$$R_{minBU} = \left[0.04984 + 6.603e^{-155.2SoC_{BU}} \right] \frac{n_{sBU}}{n_{pBU}} \quad (29)$$

$$R_{secBU} = \left[0.04669 + 0.3208e^{-21.14SoC_{BU}} \right] \frac{n_{sBU}}{n_{pBU}} \quad (30)$$

In Equations (28)–(30), SoC_{BU} is the state of charge of the BU, n_{sBU} is the number of BUs connected in series, and n_{pBU} is the number of BUs connected in parallel. As the BU was set to 60 V, 10 A, the number of series and parallel cells was determined using this voltage and current value. Similarly, the Maxwell BCAP 3000 specification was utilized for the SC [32]. The specification of the SC is depicted in Table 3. The SC voltage was set to 40 V, and the number of SC units needed to connect was determined based on this value.

Table 3. Specification of supercapacitor.

| Parameter | Value |
|---|----------------------|
| Rated voltage (V) | 2.7 |
| Rated capacitance (F) | 3000 |
| Absolute maximum current (A) | 1900 |
| SC series resistance, R_{0SC} (Ω) | 3.4×10^{-4} |
| Short-term transient resistance of SC, R_{minSC} (Ω) | 2.5×10^{-3} |
| Long-term transient resistance of SC, R_{secSC} (Ω) | 2.5×10^{-3} |

Different case studies were performed to study the performance of the designed prototype hardware model. Here, a few variables that are used in energy management must be defined. The instantaneous power consumption was assessed every 0.05 s, with the P_{bound} value set at 250 W. The BU voltage was kept at 60 V and SC voltage was set at 40 V. A rate limiter was added to the BU current controller to limit sudden changes in the BU output current, in addition to energy management.

As previously described, instead of using BU and SC, two bidirectional DC sources were used. These sources were connected to the bi-directional H bridge converter. The current output from these sources was measured using a USM-31V sensor module; then, the SoC was evaluated using for the BU using the equation:

$$SoC_{BU}(t) = SoC_{BU}(t - 1) - \frac{\Delta t * I_{BU}(t)}{3600 * C_{BU}}. \quad (31)$$

where SoC_{BU} is the state of charge of the BU, Δt is the time difference between the samples, and C_{BU} is the rated capacity of the BU. Then, using Equations (28)–(30), the internal resistance value of the BU was measured to evaluate the dynamic resistance of the BU (R_{BU}).

Similarly, for the SC, the resistance values reported in Table 3 were used to determine the resistance of the SC after determining the number of SC units to be connected in series and parallel. Then, the power split ratio was evaluated for the BU using Equation (27) for different modes of operation and then incorporated into the control loop to split the total reference current among two sources.

6.1. Case Study 1: Effect of Sudden Increase in Speed and Input Load Torque

Sharp increases in speed and load torque were tested on the designed system prototype. This study aimed to check the condition of the simultaneous change in the demanded speed and load torque on the designed system. Figure 12a shows the reference speed, while Figure 12b shows the input voltage for the magnetic brake controller. Since the load torque changed linearly with the voltage given to the brake controller, Figure 12b could be used to describe this fluctuation. Up to 70 s, the demanded speed was varied in steps and after that, load torque was also varied in steps along with the demanded speed.

Figure 12a shows that the speed instantly increased and was then sustained for a specific period (10 s or 20 s). The load torque applied to the traction motor also increased instantly in steps of 10 s or 20 s once the motor attained 500 rpm (as shown in Figure 11b). With the load torque, the speed increased further. It is seen that the speed and load torque of the system suddenly increased around 100 s, as represented in Figure 12a,b. For this change in speed and load torque, the intended system was assessed.

Figure 13a shows the speed under the characteristics for Case Study 1 with channel 4 (purple) being the actual speed and channel 3 (green) representing the reference speed. The speed is plotted as the voltage in the oscilloscope at a scale of 1 rpm/V. Even with an abrupt acceleration and change in input load torque, the traction motor could support the reference speed (represented as the zoomed view of the dotted region in Figure 13a).

The simulation results with an identical scenario shown in Figure 13b verified the speed-following capability of the experimental output.

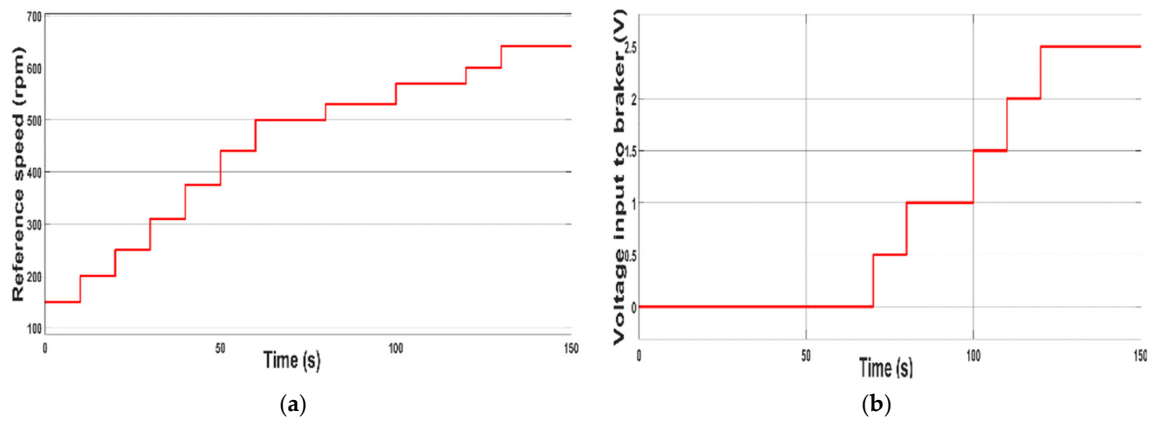
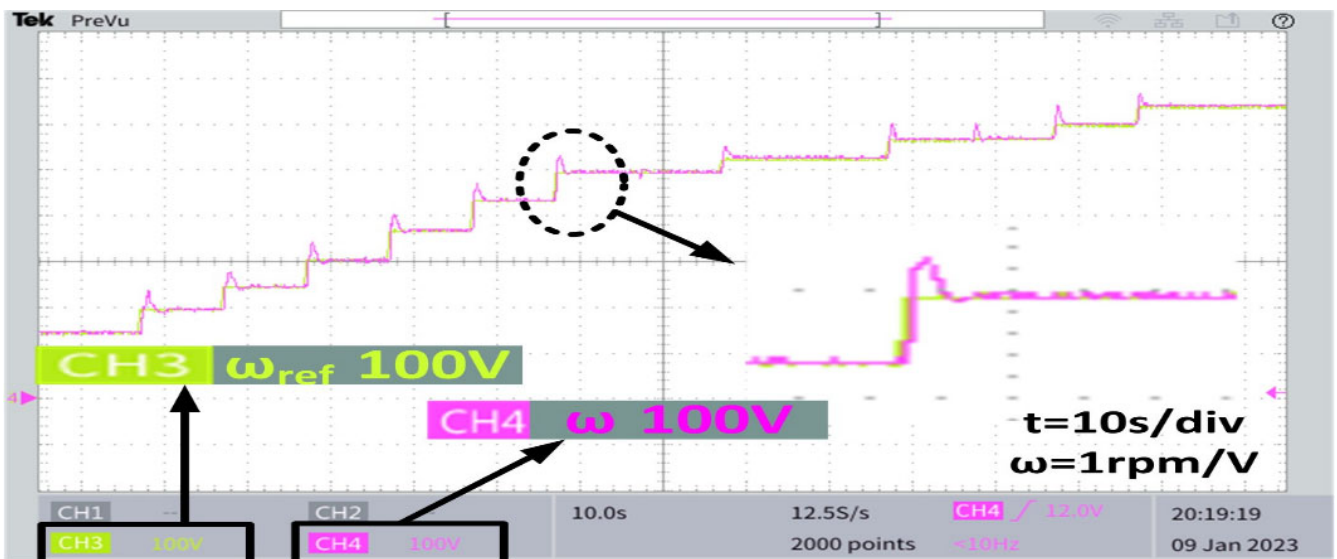
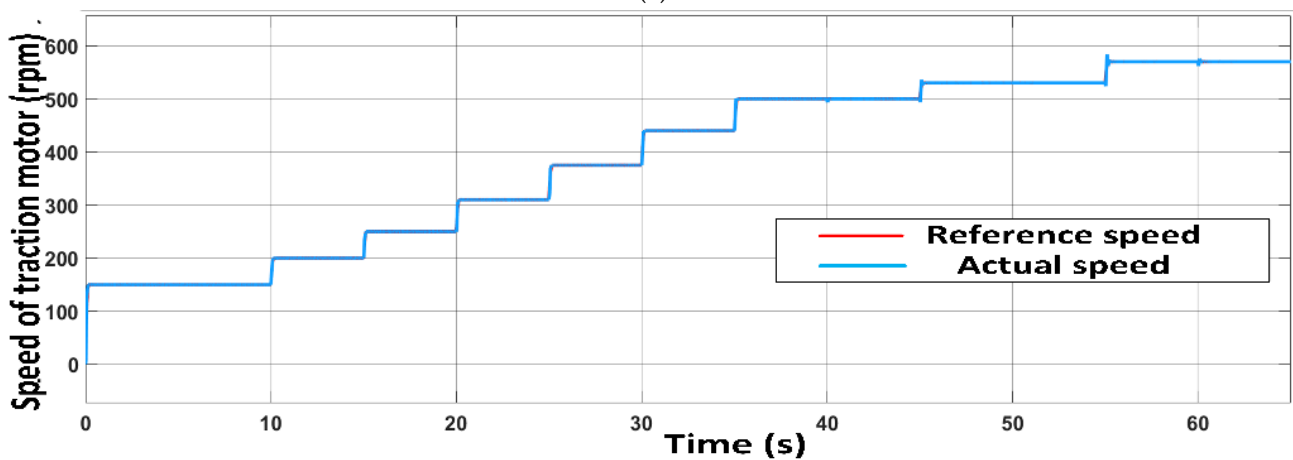


Figure 12. (a) Reference speed input for case study 1; (b) voltage input to the magnetic brake system for case study 1.



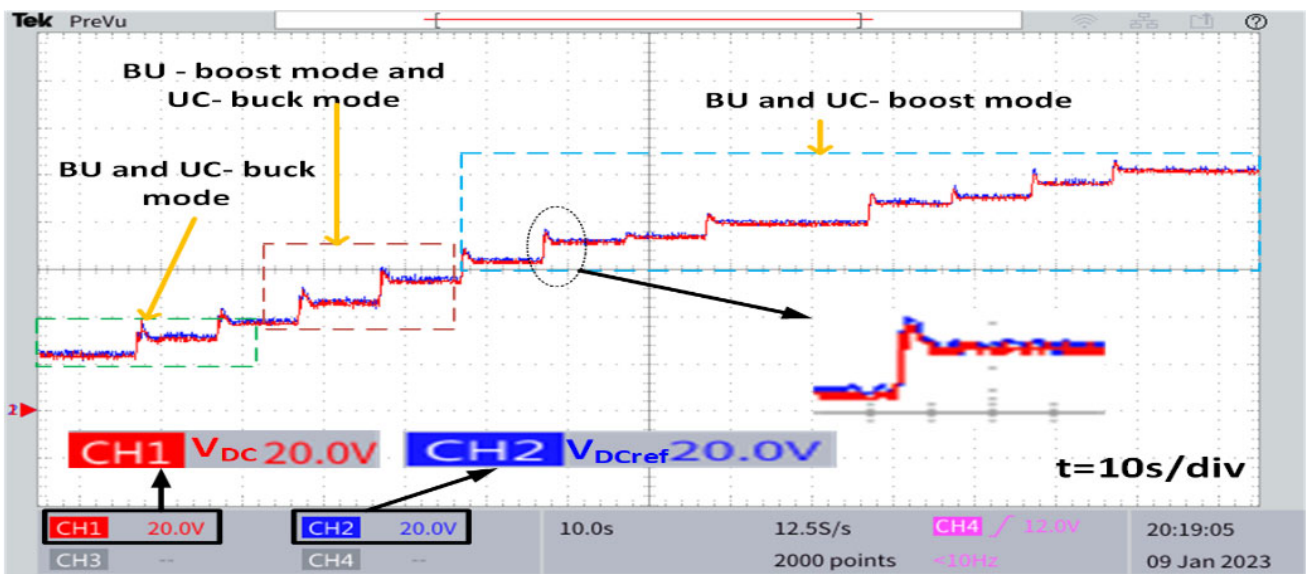
(a)



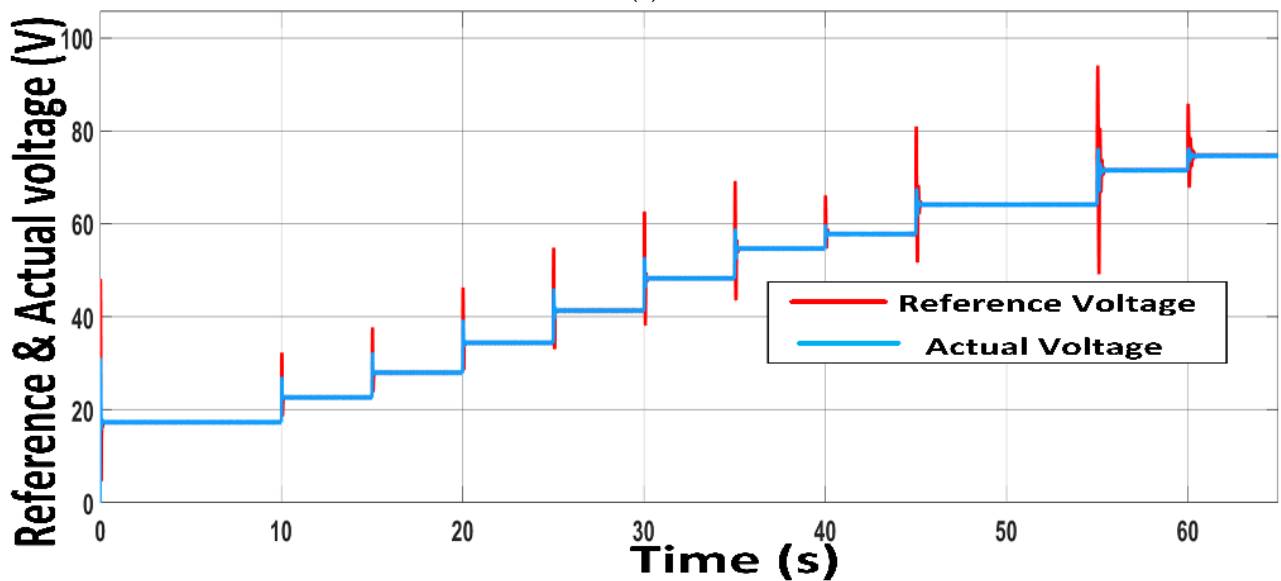
(b)

Figure 13. (a) Experimental speed follower characteristics for case study 1; (b) simulated speed follower characteristics for case study 1.

The NLSFC with a DO speed controller generated the reference armature voltage needed for the traction motor. Figure 14a shows the voltage following characteristics to prove the effectiveness of the voltage and speed controller. Channel 1 (red) shows the reference voltage generated by the speed controller and channel 2 (blue) represents the output DC voltage from the voltage controller. This voltage is fed as the armature voltage. Three areas are described in Figure 14a. The *BU* and *UC*-coupled H bridge converter ran in the buck mode when the output voltage was less than 40 V. The *BU* converter ran in the buck mode for output voltage ranges of 40 V to 60 V, while the *SC* converter worked in the boost mode. Both converters functioned as boost converters at output voltages greater than 60 V. Figure 14a shows these areas in detail. The simulated voltage following characteristic is shown in Figure 14b. The speed was directly proportional to the applied voltage, and the voltage pattern produced by the speed controller reflected this relationship.



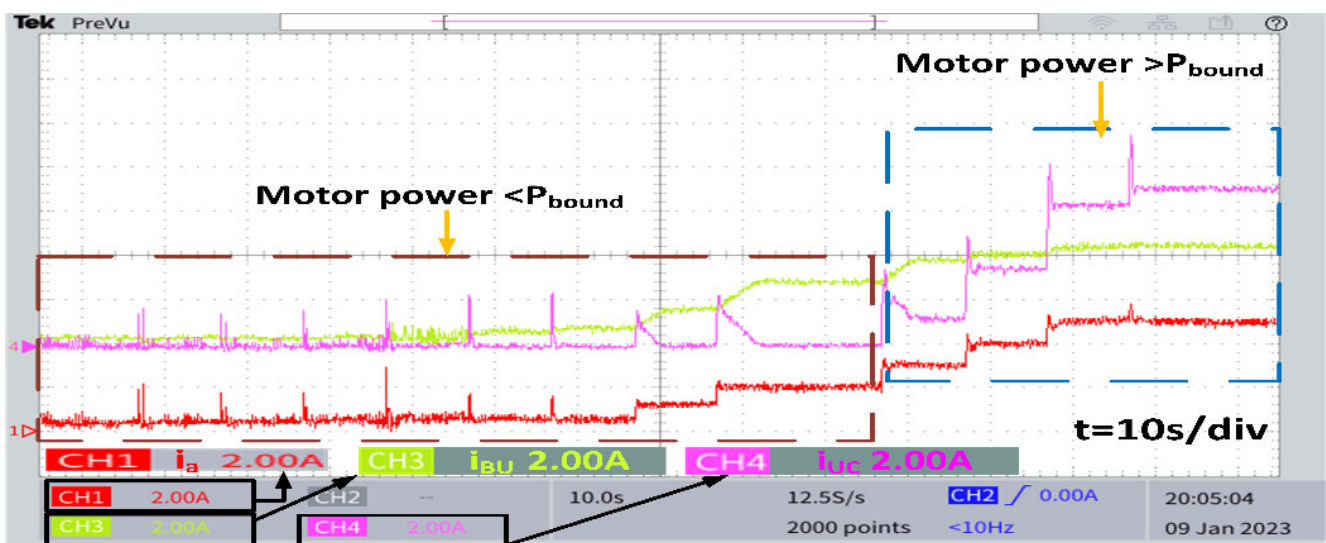
(a)



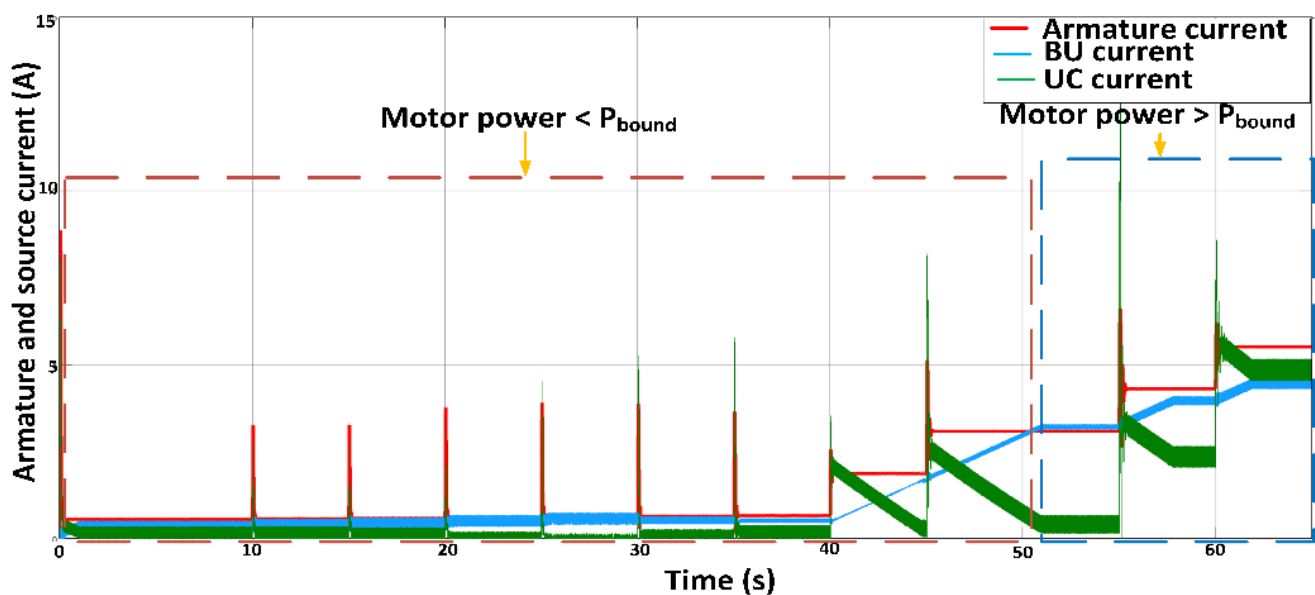
(b)

Figure 14. (a) Experimental voltage follower characteristics for case study 1; (b) simulated voltage follower characteristics for case study 1.

The energy management embedded in the control system has an impact on the current drawn from two sources. Figure 15a displays the experimental results, with the armature current output shown in channel 1 (red), the BU current output shown in channel 3 (purple), and the SC current output shown in channel 4 (green). Figure 15a makes it clear that, when the motor power was below P_{bound} , most of the current was pulled from BU. Only the immediate current demand below P_{bound} was met by the SC. Note that, while the BU current practically stayed constant outside of P_{bound} , the SC current grew as expected from the implemented EMS. As can be seen, the BU's output current was not constant within the blue rectangle region marked in Figure 15a. The resistance of the two sources determines the ratio of variation. The output of the simulated armature current and the source output current had the same characteristics as the experimental armature current, and are shown in Figure 15b.



(a)



(b)

Figure 15. (a) Experimental armature current and source currents for case study 1; (b) simulated armature current and source currents for case study 1.

Figure 16a,b, respectively, show the experimental and modeled PSR for the BU. It is obvious that the BU produced more power compared with the SC when the motor power demand was below P_{bound} , since the PSR was close to unity. The power ratio from the BU began to decline as the power demand rose and surpassed P_{bound} .

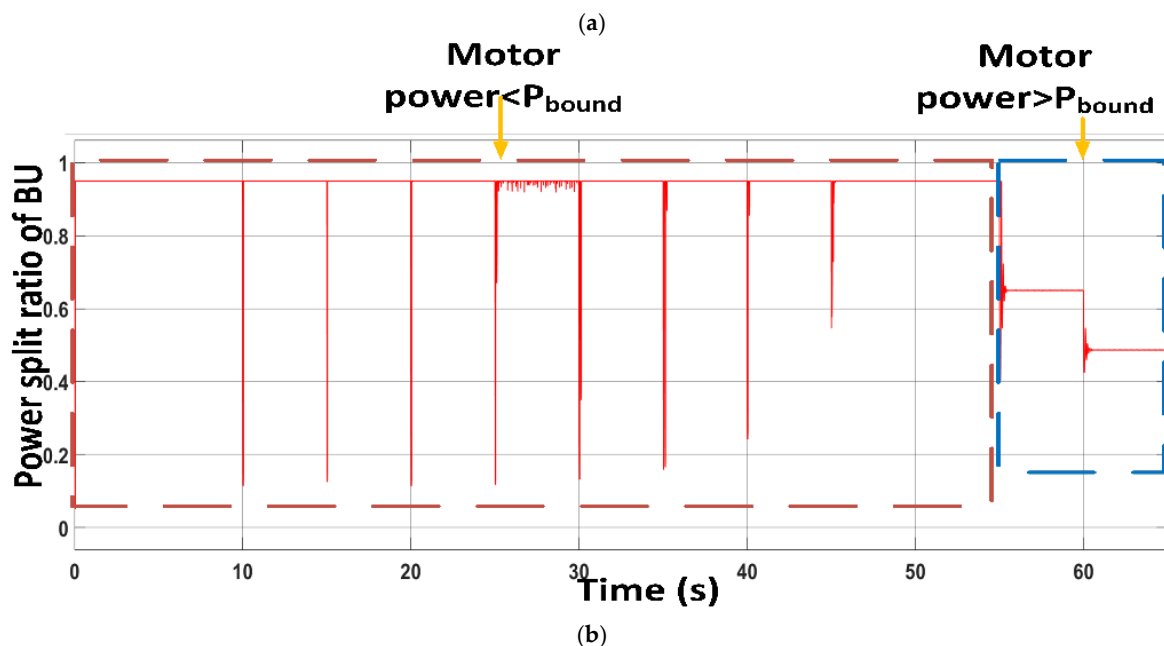
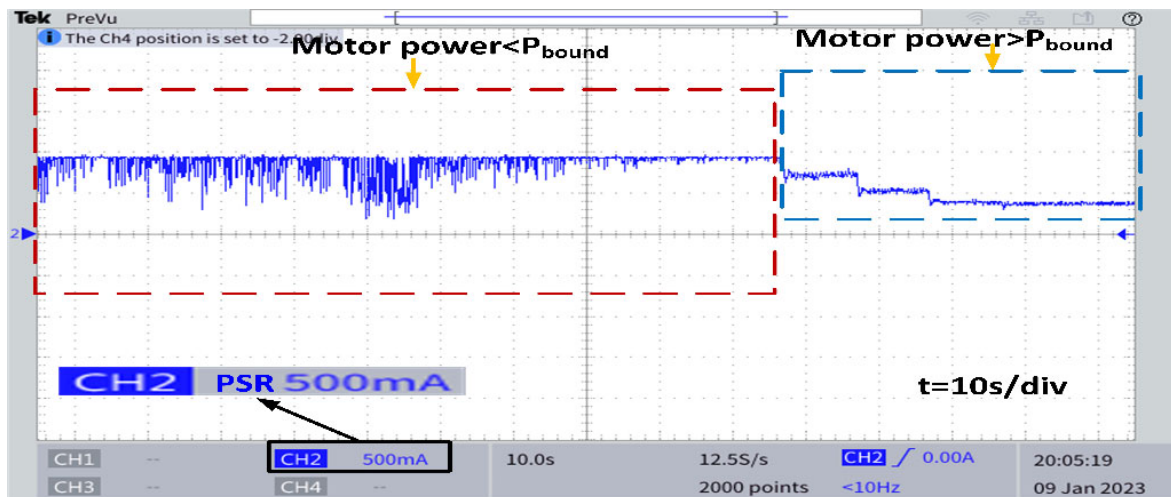


Figure 16. (a) Experimental PSR of BU for case study 1; (b) simulated PSR of BU for case study 1.

6.2. Case Study 2: Effect of Variable Acceleration and Sudden Change in Load Torque at Constant Speed

The purpose of this study was to investigate two effects: the first was the impact of variable acceleration on the system, and the second was the impact of a sudden shift in load torque at constant speed. Despite case study 1, the continuous speed change was tested with different acceleration tests without changes in load torque. Then, the load torque on the system was varied in steps to check if the system could support a constant speed. The reference speed and the input voltage (proportional to applied torque) to the magnetic brake were varied, as depicted in Figure 17a,b, respectively. As seen in Figure 17a, the motor speed increased at a varied acceleration rate for 75 s before becoming constant. The input load torque was then increased in steps while keeping the speed constant (see Figure 17b).

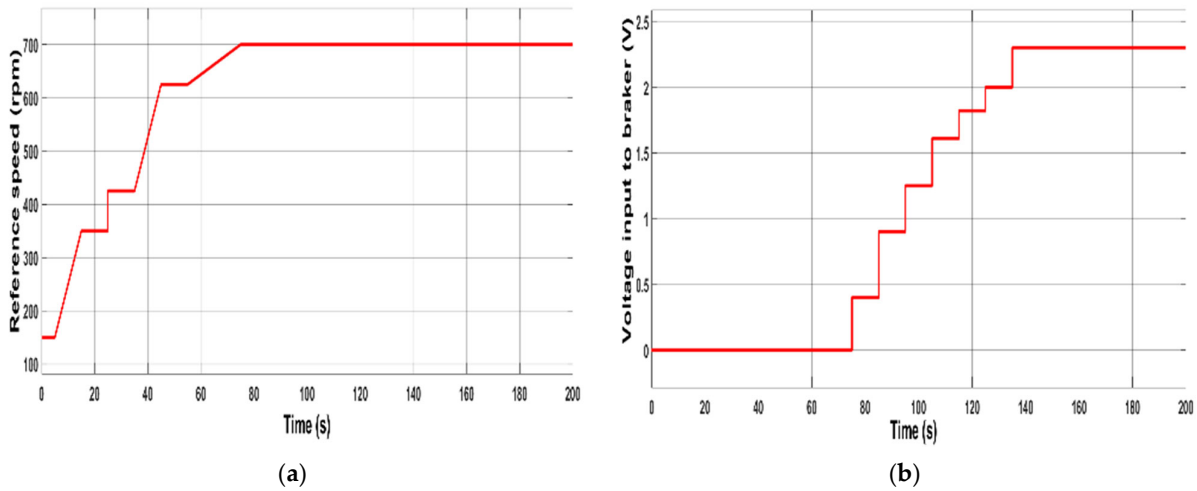


Figure 17. (a) Reference speed input for case study 2; (b) voltage input to the magnetic brake system for case study 2.

Figure 18a shows the experimental speed response characteristics, with the reference speed shown with channel 3 (green color) and the actual speed with channel 4 (purple color) of the oscilloscope. The speed obviously followed as expected, with only a few overshoots. When a sudden change in load torque occurred at a constant speed, it was seen that (zoomed view area in Figure 18a) there were little variations in speed, and this was because of the ability of the controller to support the desired speed. This claim is further verified by the speed following characteristic of the simulated system shown in Figure 18b, with identical settings to those of the system prototype.

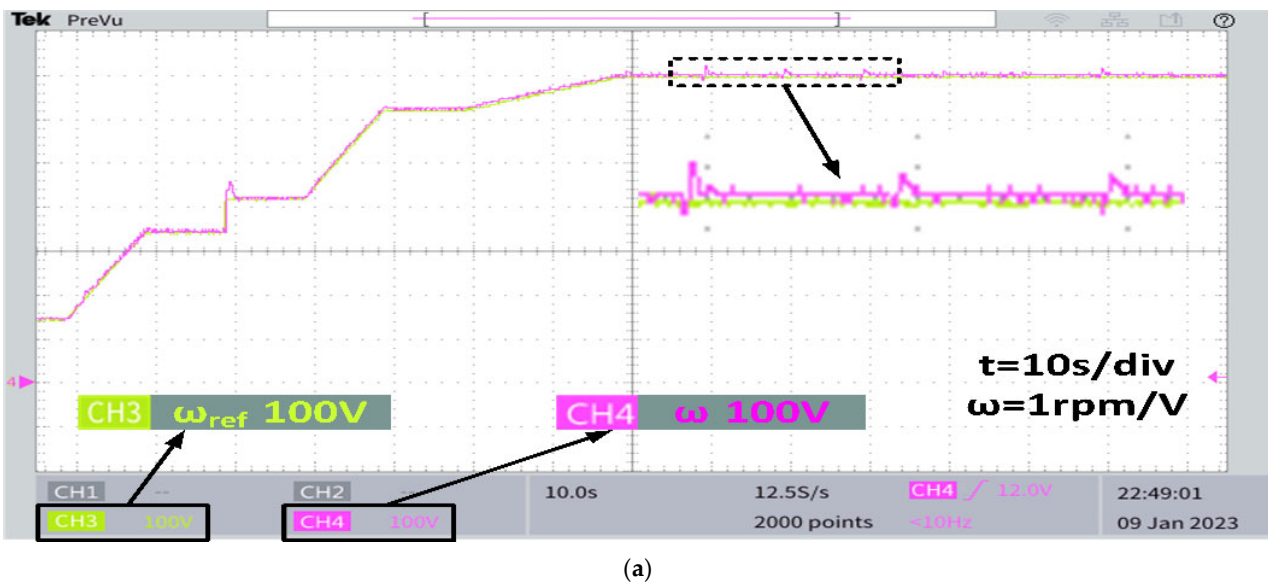


Figure 18. Cont.

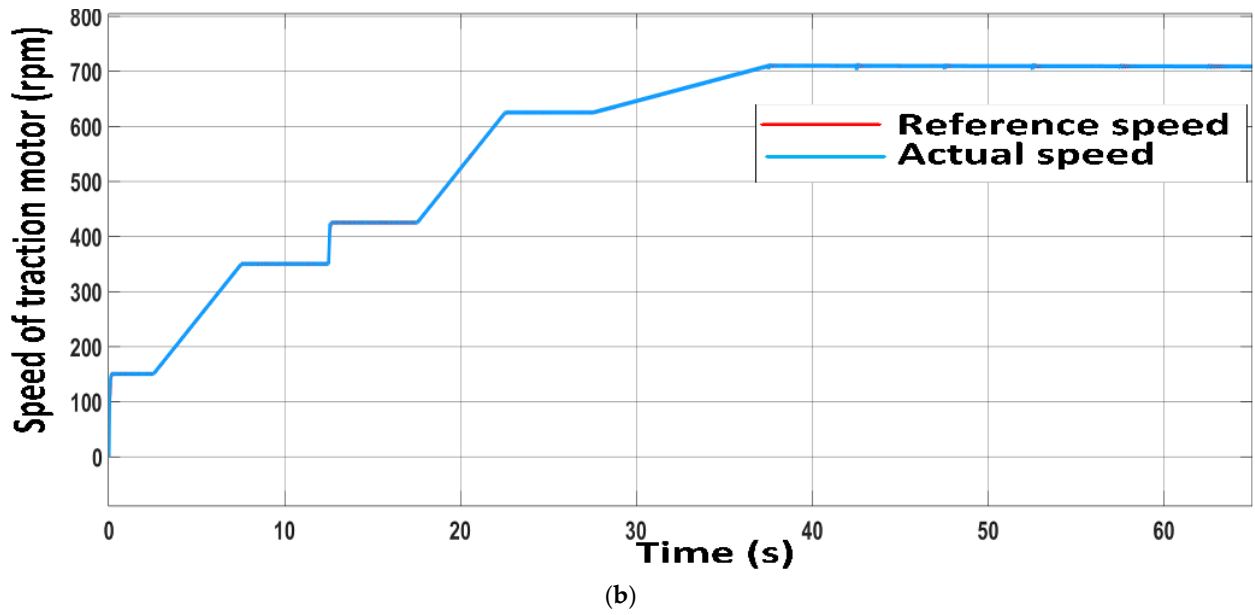


Figure 18. (a) Experimental speed follower characteristics for case study 2; (b) simulated speed follower characteristics for case study 2.

A similar pattern was observed for the generated reference voltage, as shown in Figure 19a. From the figure, it can be observed that a sudden rise in the load torque at constant speed caused a dynamic change (increase) in the generated reference voltage. This added armature voltage was necessary to compensate for the voltage drop due to the increase in armature current. The simulated voltage characteristics of the system also shown in Figure 19b confirm the experimental outcome.

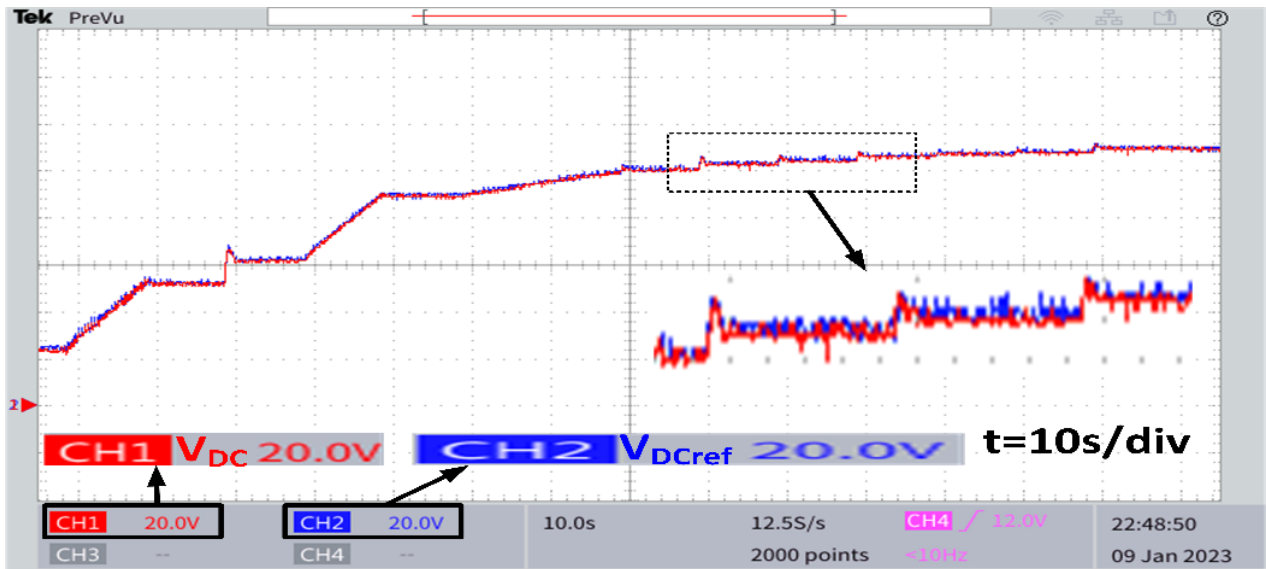


Figure 19. Cont.

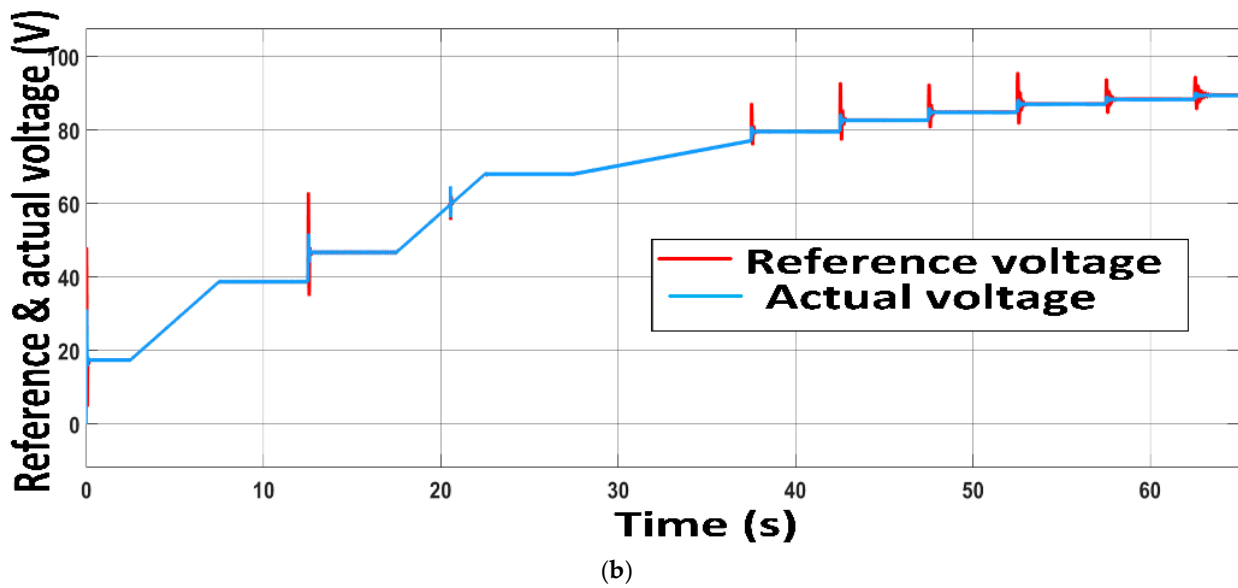


Figure 19. (a) Experimental voltage follower characteristics for case study 2; (b) simulated voltage follower characteristics for case study 2.

The results obtained from the experiment for sources and armature currents are shown in Figure 20a. As can be seen in Figure 20a, the load torque increased as the armature current (channel 1) rose. Most of the current demand was satisfied by the BU (channel 3) when the power demand at the motor side was less than P_{bound} . The SC in this region could only meet the need for instantaneous current (channel 4), and hence, instantaneous power. It is clear that the SC current grew significantly, whereas the BU current changed only slightly with increasing motor power demand. A similar observation is noted with simulated current characteristics, as depicted in Figure 20b.

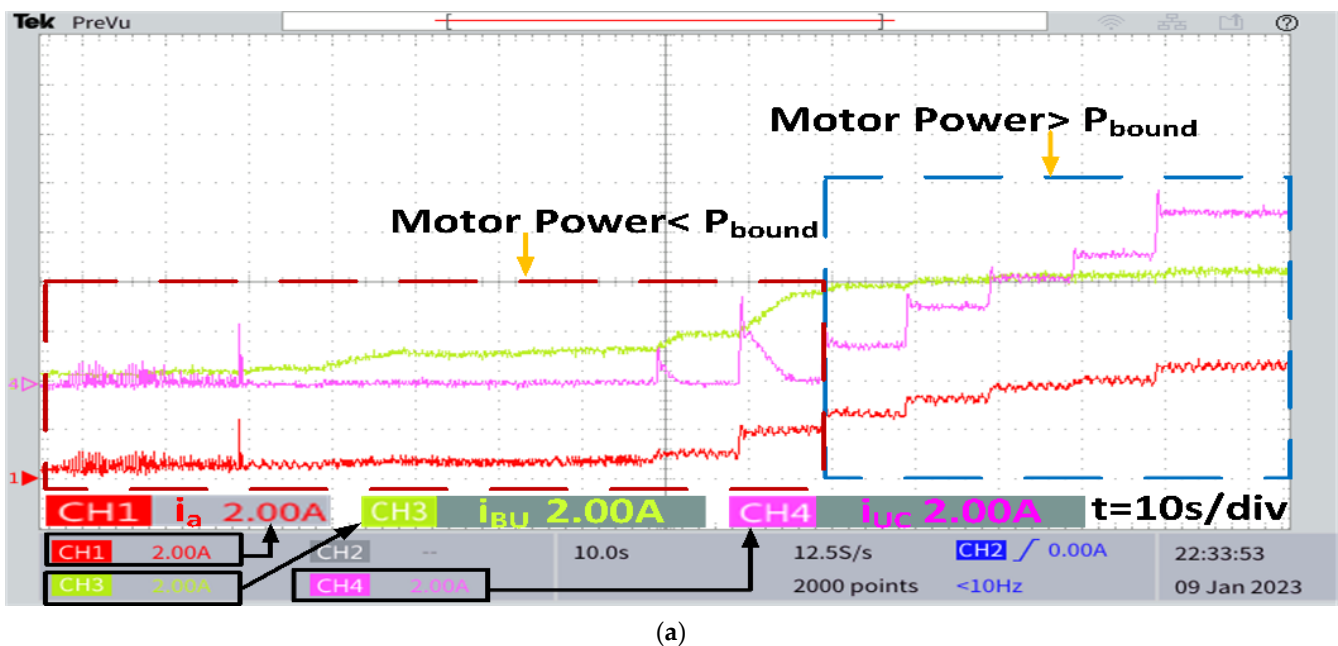


Figure 20. Cont.

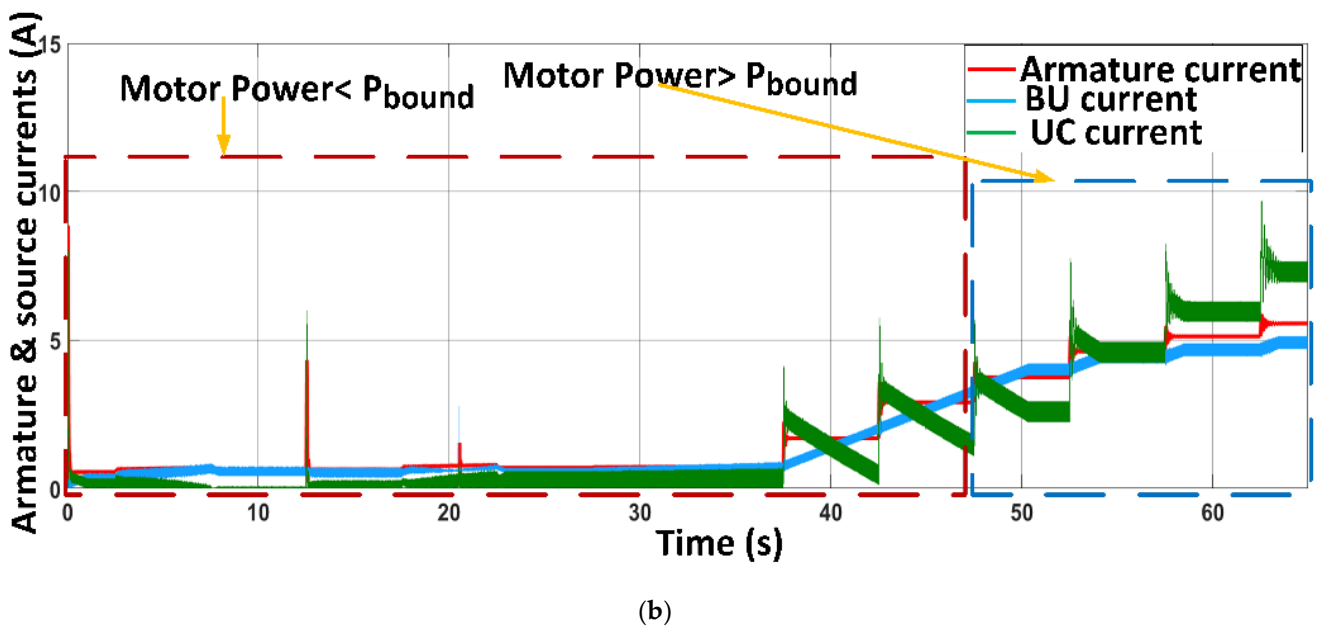
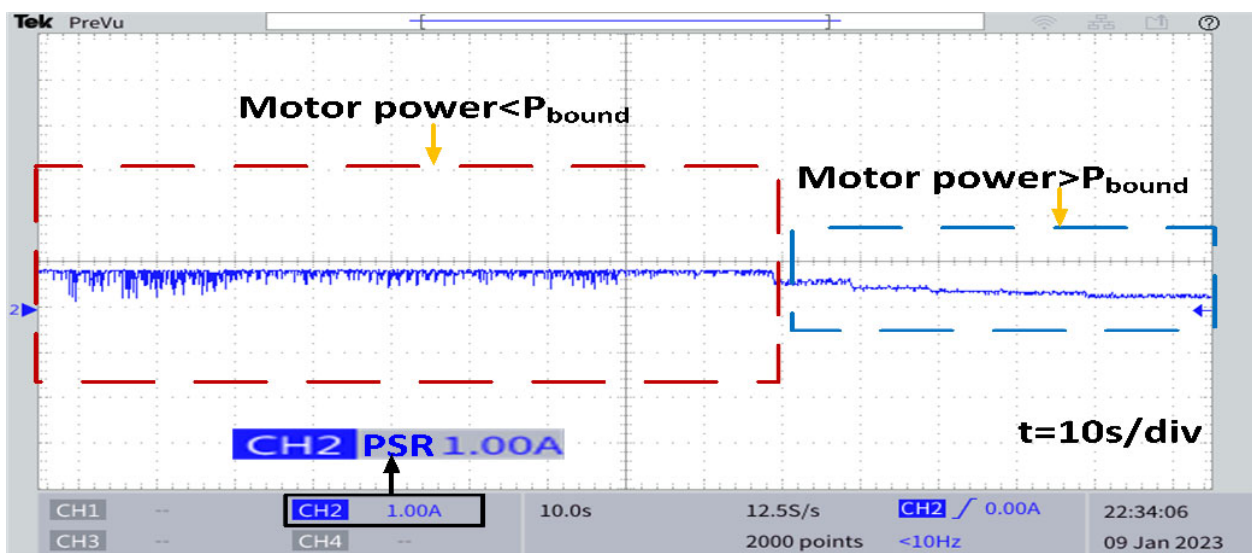


Figure 20. (a) Experimental armature current and source currents for case study 2; (b) simulated armature current and source currents for case study 2.

The experimental and simulated PSRs of the *BU* are depicted in Figure 21a,b respectively. As can be observed, when the power demand at the motor side was less than P_{bound} , the *BU* PSR generally remained at unity. This only deviated (PSR dropped below one) when the rate of change in acceleration varied. The PSR dropped to values less than one once the motor power surpassed the P_{bound} value, creating a characteristic that was the exact opposite of the armature source current. As a result, the PSR of the *BU* declined with increasing armature current, showing that most of the region’s current requirement was met by SC.



(a)

Figure 21. Cont.

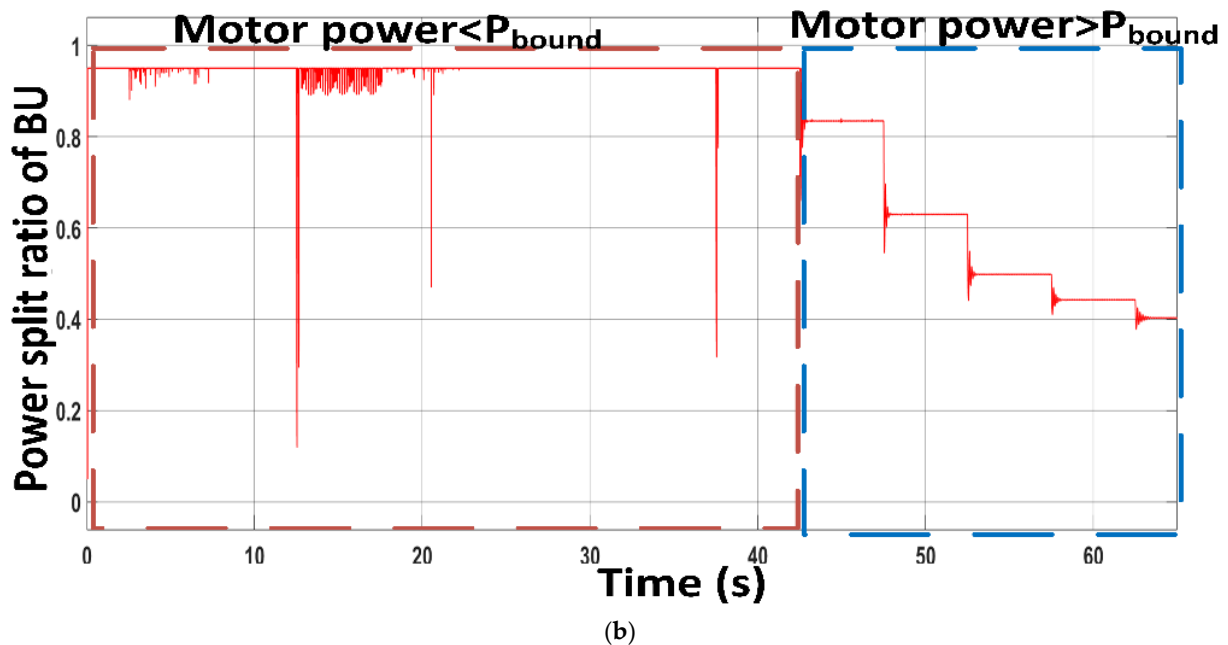


Figure 21. (a) Experimental PSR of BU for case study 2; (b) simulated PSR of BU for case study 2.

6.3. Case Study 3: Effect of Regenerative Braking

The first two case studies are an illustration of the operation of the system in the motoring mode. However, this study aimed to show how well the converters and controller worked when recovering braking energy. That is, the operation of the system when the demanded speed was suddenly reduced, i.e., the braking mode. For this case, the reference speed input was generated as shown in Figure 22. Figure 23a,b, respectively, display the experimental and simulated speed following characteristics. The reference speed is shown in channel 3 (green color) and the speed output in channel 4 (purple color) with a scale of 1 rpm/V in Figure 23a. The experimental results shown in Figure 23a clearly show that the system can effectively follow the desired speed, like the results obtained with simulation, as shown in Figure 23b.

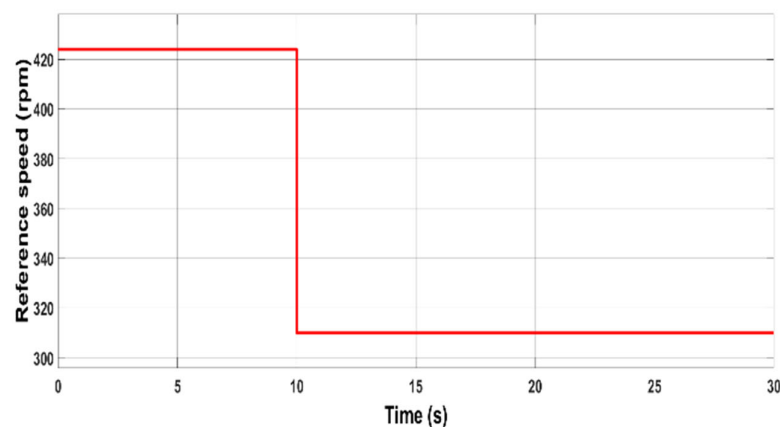
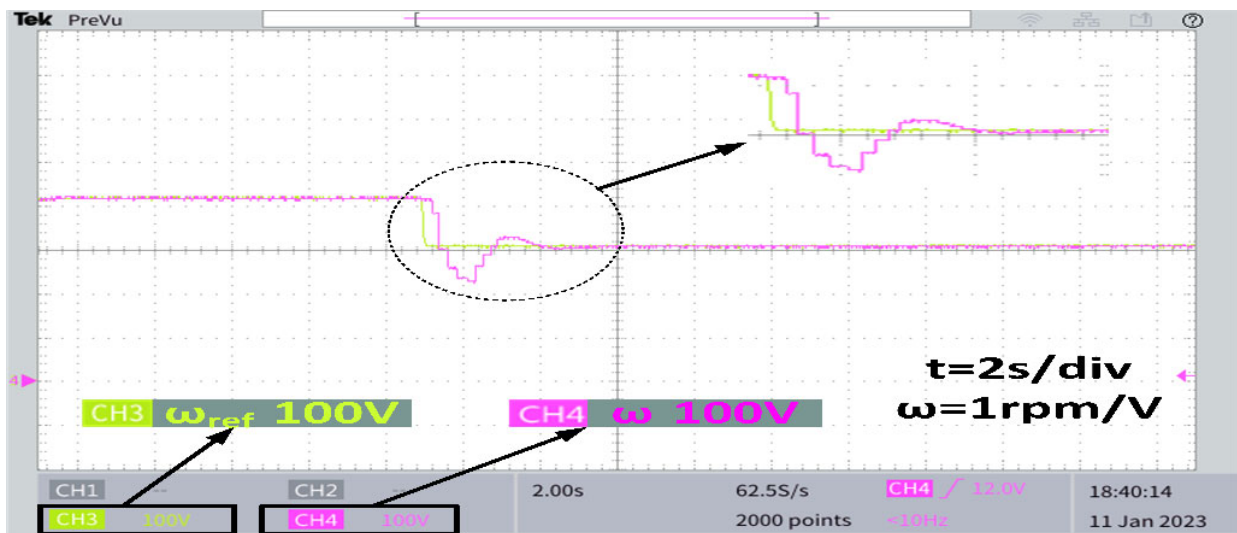
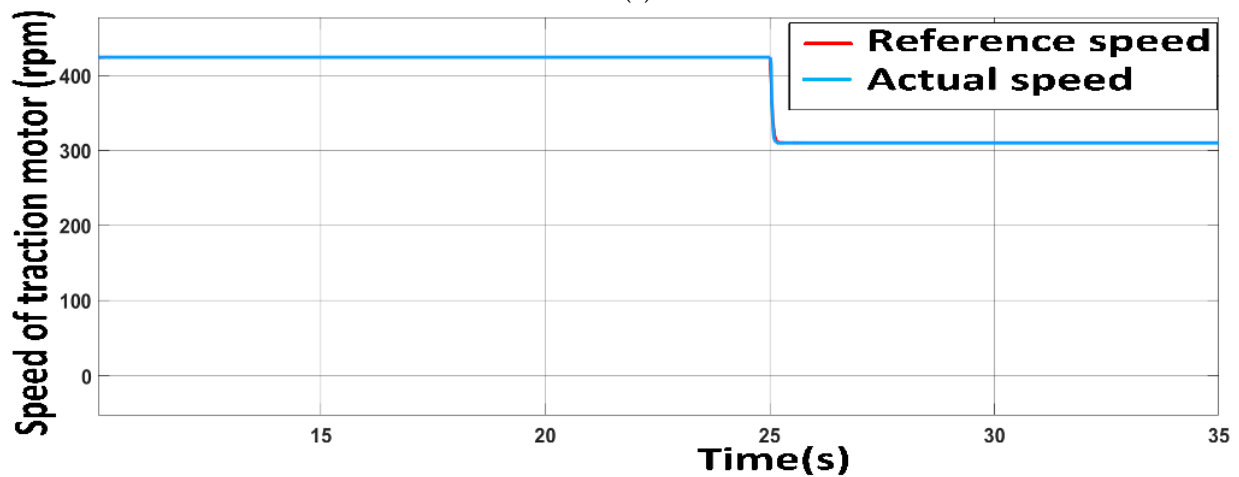


Figure 22. Reference speed input for case study 3.



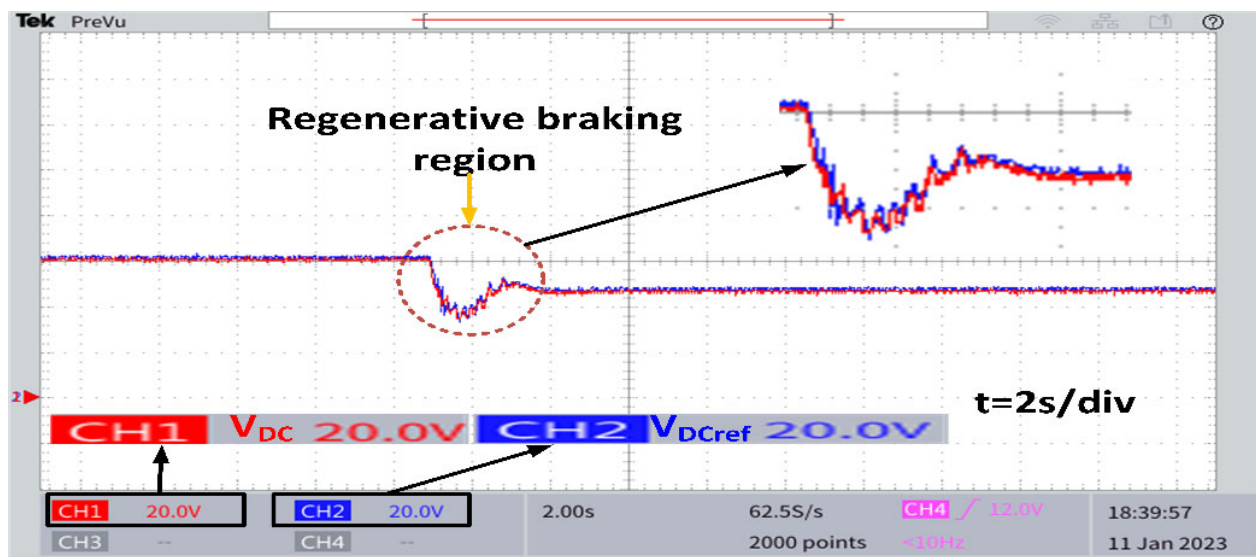
(a)



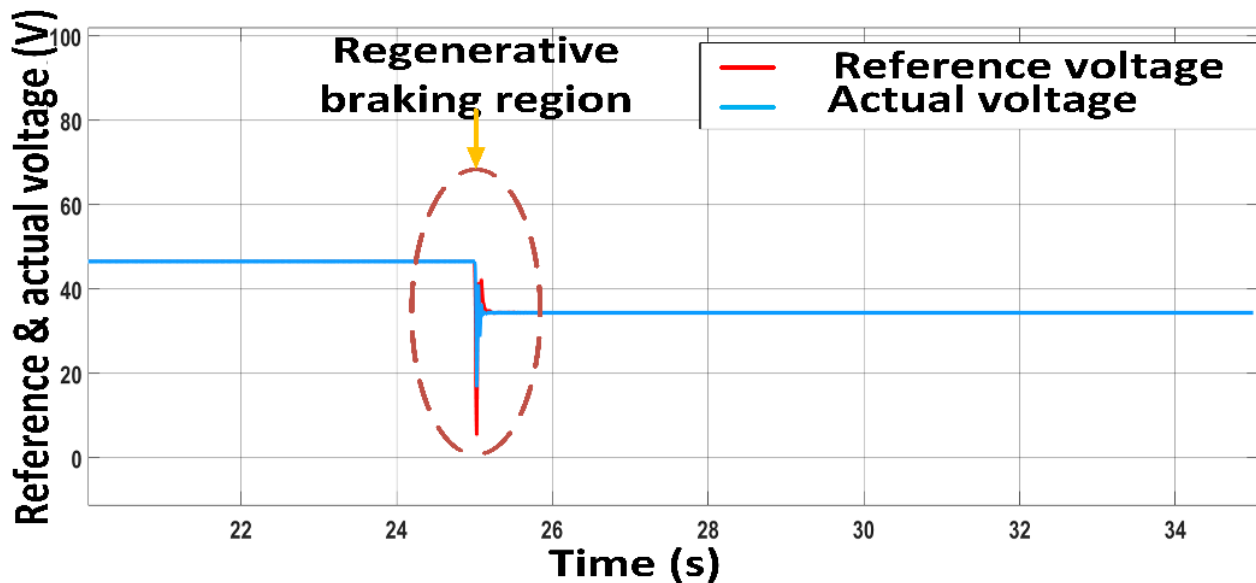
(b)

Figure 23. (a) Experimental speed follower characteristics for case study 3; (b) simulated speed follower characteristics for case study 3.

The reference voltage generated by the non-linear speed controller and the voltage output at the DC link capacitor are displayed in Figure 24a for the developed hardware system. With a sudden reduction in speed, the controller managed to reduce the voltage demand at the motor side creating regenerative braking action, as shown in Figure 24a. This action was also well verified by the simulation results shown in Figure 24b.



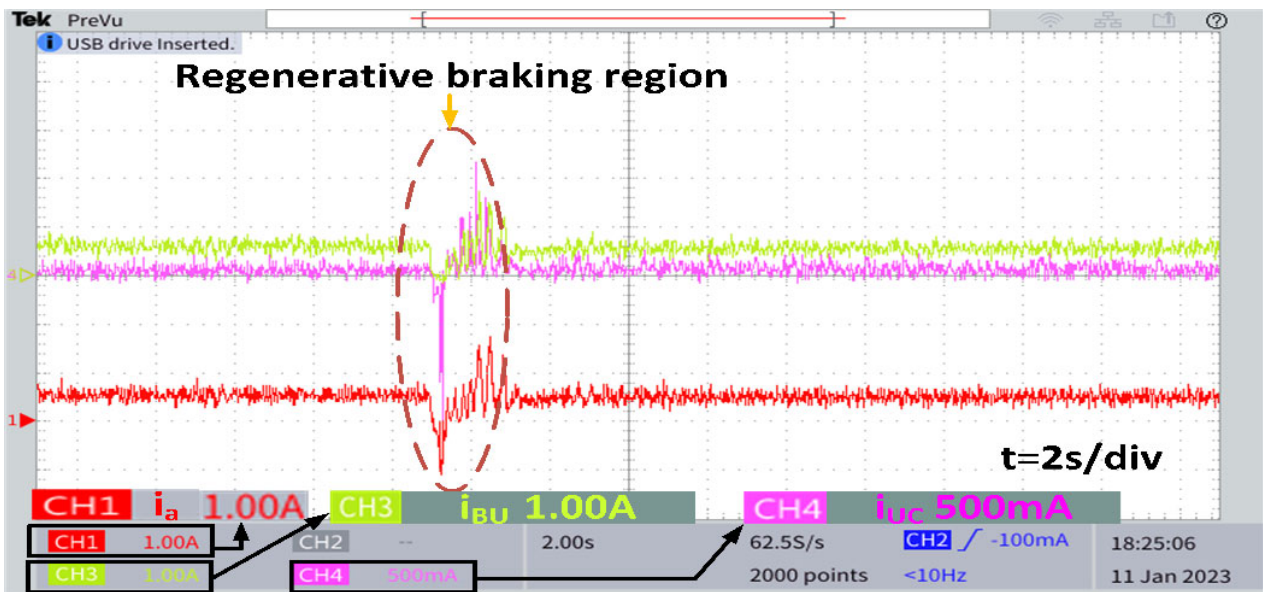
(a)



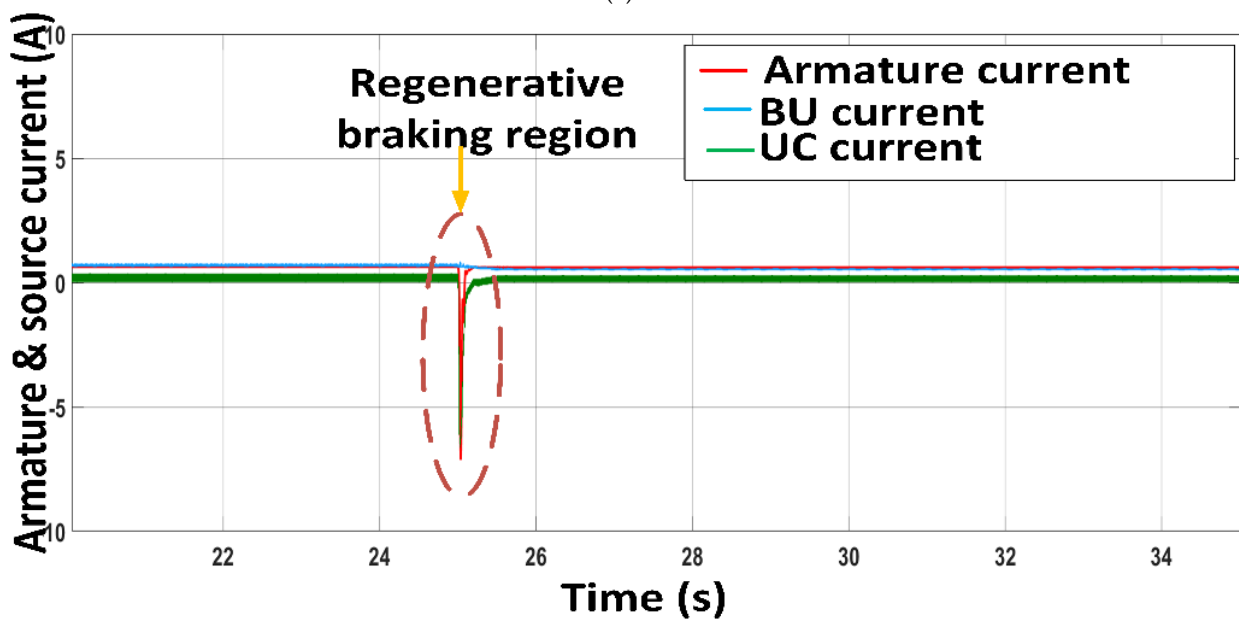
(b)

Figure 24. (a) Experimental voltage follower characteristics for case study 3; (b) simulated voltage follower characteristics for case study 3.

The armature current (channel 1), *BU* current (channel 3), and *SC* current (channel 4) are shown in Figure 25a for the experimental system. It is noted that, following the energy management used, the *SC* drew much of the reverse current. Thus, the overall system could recover the braking energy. A similar observation was found for the simulated system, as depicted in Figure 25b.



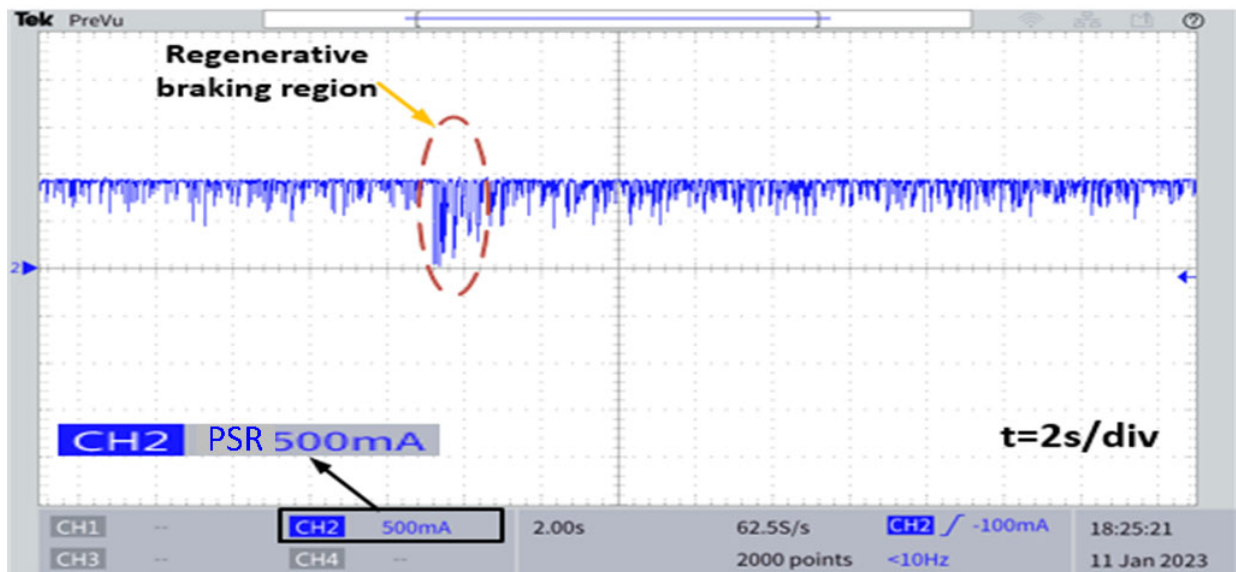
(a)



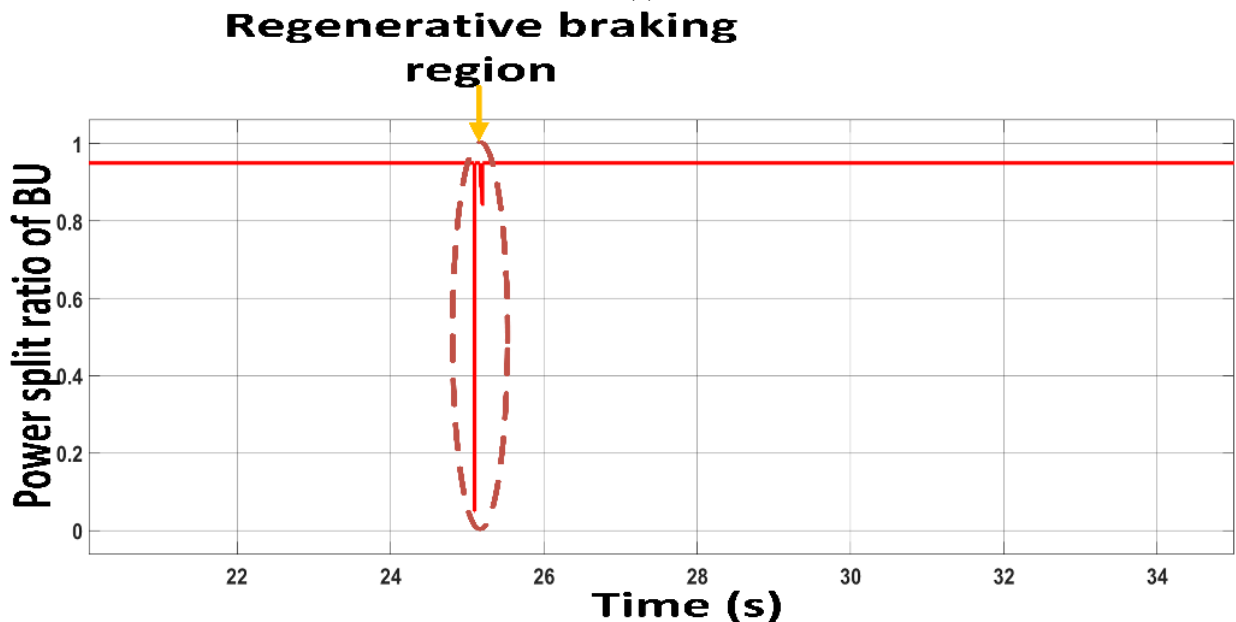
(b)

Figure 25. (a) Experimental armature current and source currents for case study 3; (b) simulated armature current and source currents for case study 3.

The PSR of the BU is displayed in Figure 26a,b for the experimented and simulated systems, respectively. The braking regions are labeled with a circle. It is noticeable that the PSR drastically fell from unity, and this enabled the quick response of the SC. In this region, the demand from the SC increased and was thus capable of recovering the current.



(a)



(b)

Figure 26. (a) Experimental PSR of BU for case study 3; (b) simulated PSR of BU for case study 3.

6.4. Validation of the Method Used with Fine-Tuned PI Controller

From the three case studies, it was verified that the developed hardware prototype could follow the demanded speed and load torque. For Case Study 1, where the system experienced a quick change in speed and load torque, the controller's performance was evaluated. The settling time, also known as the time it took for the system to stabilize within a 1% tolerance band after an input stimulus, was discovered to be 0.75 s. The outcome showed that the controller ran efficiently in both the driving and regenerative braking modes. The entire system could keep the intended properties, despite abrupt changes in speed and load torque with little disruption.

For the validation of the proposed system, the NLSFC with DO was replaced with a fine-tuned PI controller and the simulation study was performed to compare the speed follower characteristics for case study 1 and case study 2. For a better understanding of the performance, the simulation was executed for 30 s. The performance comparison for

case study 1 with NLSFC with DO is depicted in Figure 27a and with PI controller in Figure 27b. The speed follower characteristics for case study 2 are presented in Figure 28a for the NLSFC controller and in Figure 28b for the fine-tuned PI controller.

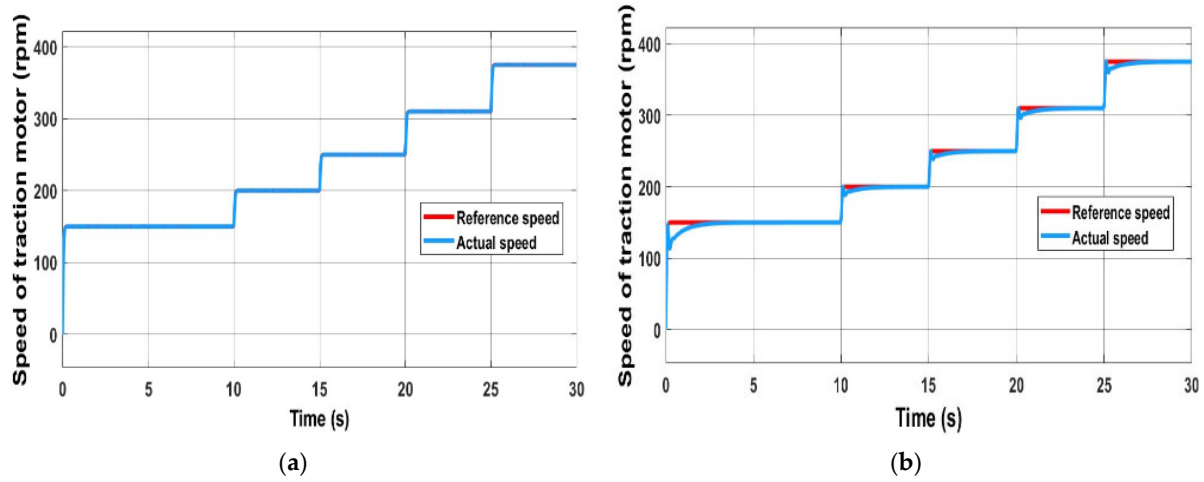


Figure 27. Speed follower characteristics for case study 1 with (a) NLSFC with DO; (b) fine-tuned PI controller.

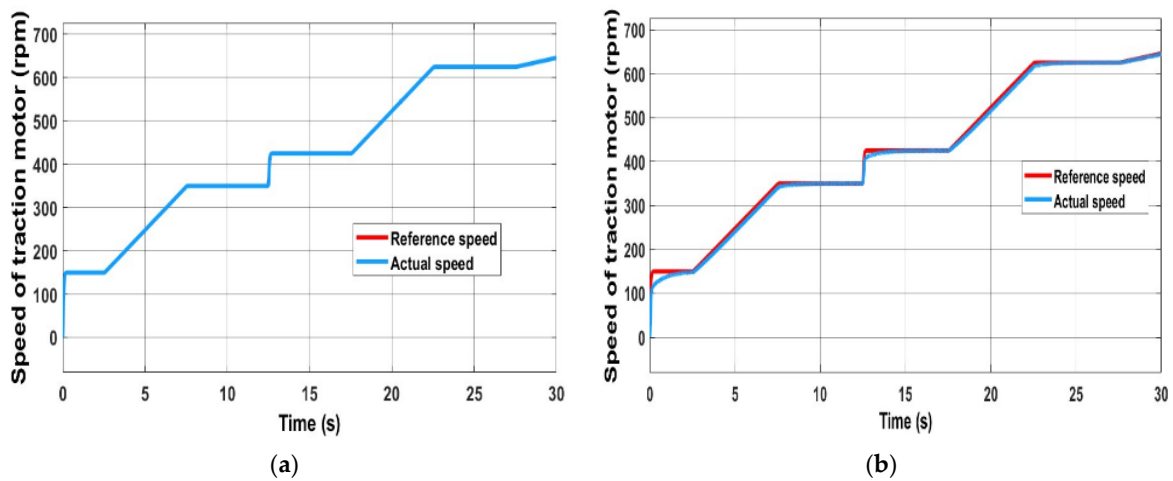


Figure 28. Speed follower characteristics for case study 2 with (a) NLSFC with DO; (b) fine-tuned PI controller.

The transient performance indicators were calculated for comparison with the two controllers—NLSFC with DO and fine-tuned PI controller. The settling time within a 1% tolerance band and steady state error (SSE) were evaluated for two case studies and are presented in Table 4 for comparison.

Table 4. Transient performance indicators for validation of proposed controller with fine-tuned PI controller.

| Parameter | Case Study 1 | | Case Study 2 | |
|-------------------|---------------|---------------|---------------|---------------|
| | NLSFC with DO | PI Controller | NLSFC with DO | PI Controller |
| Settling time (s) | 0.75 | 1.4 | 0.25 | 1.15 |
| SSE (rpm) | 0.002 | 0.5 | 0.002 | 0.4 |

7. Conclusions

This paper showed the real time control of an EV traction motor with two energy sources, namely a *BU* and an *SC*. The NLSFC speed controller with *DO* and a new adaptive energy management algorithm was tested with a hardware model. A detailed explanation of each component used in the experiment with a way to extract values for developing the control system and energy management using the real-time controller *dSpace1202* is presented. Depending on the motor rating, the system was tested under a variety of speed and load torque conditions. Furthermore, the system could be reproduced to higher ratings and as a benchmark model.

Author Contributions: Conceptualization, A.P. and H.S.; methodology, A.P.; software, A.P. and H.S.; validation, A.P., H.S. and R.E.; formal analysis, A.P.; investigation, A.P.; resources, H.S.; writing—original draft preparation, A.P.; writing—review and editing, H.S., M.A. and A.W.; supervision, H.S. and R.E.; funding acquisition, H.S. All authors have read and agreed to the published version of the manuscript.

Funding: This research was supported by the Strategic Research Program, UAEU. (Project title: “Optimal Design and Real-Time Control of a Hybrid Electric Vehicle with Adaptive Energy Management and Non-Linear State Feedback Control Schemes”) under Grant G00004216.

Data Availability Statement: Not applicable.

Conflicts of Interest: The authors declare no conflict of interest.

References

- Panday, A.; Bansal, H.O. A review of optimal energy management strategies for hybrid electric vehicle. *Int. J. Veh. Technol.* **2014**, *2014*, 160510. [CrossRef]
- Bansal, U.K.; Narvey, R. Speed Control of DC Motor Using Fuzzy PID Controller. *Adv. Electron. Electr. Eng.* **2013**, *3*, 1209–1220. Available online: <http://www.ripublication.com/aeee.htm> (accessed on 19 April 2023).
- Mondal, R.; Mukhopadhyay, A.; Basak, D. Embedded System of DC Motor Closed Loop Speed Control based on 8051 Microcontroller. In Proceedings of the 1st International Conference on Computational Intelligence: Modeling Techniques and Applications (CIMTA), Kalyani, India, 27–28 September 2013; Volume 10, pp. 840–848. [CrossRef]
- Nagarajan, R.; Sathishkumar, S.; Balasubramani, K.; Boobalan, C.; Naveen, S.; Sridhar, N. Chopper Fed Speed Control of DC Motor Using PI Controller. *IOSR J. Electr. Electron. Eng.* **2016**, *11*, 65–69.
- Liceaga-Castro, J.U.; Siller-Alcalá, I.I.; Jaimes-Ponce, J.; Alcántara-Ramírez, R.A.; Arévalo Zamudio, E. Identification and Real Time Speed Control of a Series DC Motor. *Math. Probl. Eng.* **2017**, *2017*, 7348263. [CrossRef]
- Salman, S.A.; Obaid, Z.A.; Hameed, H.S. Stability and performance evaluation of the speed control of DC motor using state-feedback controller. *Indones. J. Electr. Eng. Comput. Sci.* **2021**, *22*, 1372–1378. [CrossRef]
- Sharifian, M.B.B.; Rahnavard, R.; Delavari, H. Velocity Control of DC Motor Based Intelligent Methods and Optimal Integral State Feed Back Controller. *Int. J. Comput. Theory Eng.* **2009**, *1*, 81–84. [CrossRef]
- Alhanjouri, M. Speed Control of DC Motor Using Artificial Neural Network. *Int. J. Sci. Res.* **2017**, *7*, 2140–2148.
- Liceaga-Castro, J.U.; Siller-Alcalá, I.I.; Alcántara-Ramírez, R.A.; Román, J.D.G. PI Speed Control with Reverse Motion of a Series DC Motor Based on the Noise Reduction Disturbance Observer. *Actuators* **2022**, *11*, 117. [CrossRef]
- Tripathi, R.P.; Singh, A.K.; Gangwar, P.; Verma, R.K. Sensorless speed control of DC motor using EKF estimator and TSK fuzzy logic controller. *Automatika* **2022**, *63*, 338–348. [CrossRef]
- Maheswararao, C.U.; Babu, Y.K.; Amaresh, K. Sliding Mode Speed Control of a DC Motor. In Proceedings of the 2011 International Conference on Communication Systems and Network Technologies, Katra, India, 3–5 June 2011. [CrossRef]
- Nasri, A.; Hazzab, A.; Bousserhane, I.K.; Hadjeri, S.; Sicard, P. Fuzzy-Sliding Mode Speed Control for Two Wheels Electric Vehicle Drive. *J. Electr. Eng. Technol.* **2009**, *4*, 499–509. [CrossRef]
- Wen, C.-C.; Chung, C.-W.; Wang, H.-M.; Chang, Y. Design of the fuzzy sliding mode controller for DC motor. In Proceedings of the 2013 Second International Conference on Robot, Vision and Signal Processing, Kitakyushu, Japan, 10–12 December 2013; pp. 196–199. [CrossRef]
- Liu, Y.C.; Laghrouche, S.; Depernet, D.; N'Diaye, A.; Djerdir, A.; Cirrincione, M. Super-twisting sliding-mode observer-based model reference adaptive speed control for PMSM drives. *J. Frankl. Inst.* **2023**, *360*, 985–1004. [CrossRef]
- Jiang, D.; Fang, Y.; Fei, J. An Extended-State Observer Based on Smooth Super-Twisting Sliding-Mode Controller for DC-DC Buck Converters. *Mathematics* **2023**, *11*, 2835. [CrossRef]
- Yan, Y.; Yang, J.; Sun, Z.; Li, S.; Yu, H. Non-linear-disturbance-observer-enhanced MPC for motion control systems with multiple disturbances. *IET Control Theory Appl.* **2020**, *14*, 63–72. [CrossRef]

17. Apte, A.A.; Joshi, V.A.; Walambe, R.A.; Godbole, A.A. Speed control of PMSM using disturbance observer. *IFAC-PapersOnLine* **2016**, *49*, 308–313. [[CrossRef](#)]
18. González-Castaño, C.; Restrepo, C.; Kouro, S.; Vidal-Idiarte, E.; Calvente, J. A bidirectional versatile buck–boost converter driver for electric vehicle applications. *Sensors* **2021**, *21*, 5712. [[CrossRef](#)]
19. Kandilli, İ. Real-time speed controlling of a DC motor using fuzzy logic controller. *Pamukkale Univ. J. Eng. Sci.* **2017**, *23*, 543–549. [[CrossRef](#)]
20. Hernández-Márquez, E.; García-Sánchez, J.R.; Silva-Ortigoza, R.; Antonio-Cruz, M.; Hernández-Guzmán, V.M.; Taud, H.; Marcelino-Aranda, M. Bidirectional tracking robust controls for a DC/DC buck converter–DC motor system. *Complexity* **2018**, *2018*, 1260743. [[CrossRef](#)]
21. Abdelaal, A.S.; Mukhopadhyay, S.; Rehman, H. Battery Energy Management Techniques for an Electric Vehicle Traction System. *IEEE Access* **2022**, *10*, 84015–84037. [[CrossRef](#)]
22. Islam, M.M.; Siffat, S.A.; Ahmad, I.; Liaquat, M.; Khan, S.A. Adaptive Nonlinear Control of Unified Model of Fuel Cell, Battery, Ultracapacitor and Induction Motor Based Hybrid Electric Vehicles. *IEEE Access* **2021**, *9*, 57486–57509. [[CrossRef](#)]
23. Devi Vidhya, S.; Balaji, M. Hybrid fuzzy PI controlled multi-input DC/DC converter for electric vehicle application. *Automatika* **2020**, *61*, 79–91. [[CrossRef](#)]
24. Kakouche, K.; Rekioua, T.; Mezani, S.; Oubelaid, A.; Rekioua, D.; Blazek, V.; Prokop, L.; Misak, S.; Bajaj, M.; Ghoneim, S.S.M. Model Predictive Direct Torque Control and Fuzzy Logic Energy Management for Multi Power Source Electric Vehicles. *Sensors* **2022**, *22*, 5669. [[CrossRef](#)] [[PubMed](#)]
25. Oubelaid, A.; Alharbi, H.; Humayd, A.S.B.; Taib, N.; Rekioua, T.; Ghoneim, S.S.M. Fuzzy-Energy-Management-Based Intelligent Direct Torque Control for a Battery—Supercapacitor Electric Vehicle. *Sustainability* **2022**, *14*, 8407. [[CrossRef](#)]
26. Sultan, G.A.; Sheet, A.F.; Ibrahim, S.M.; Farej, Z.K. Speed control of DC motor using fractional order PID controller based on particle swarm optimization. *Indones. J. Electr. Eng. Comput. Sci.* **2021**, *22*, 1345–1353. [[CrossRef](#)]
27. Alnaib, A.M.T.I.; Sultan, N.S.; Mahmood, O.T. Design a Fuel cell based drive DC motor for an electric vehicle applications. *Int. J. Eng. Technol.* **2018**, *7*, 2081–2087. [[CrossRef](#)]
28. Praptodiyono, S.; Maghfiroh, H.; Saputro, J.S.; Ramelan, A. Integral State Feedback Control Using Linear Quadratic Gaussian in DC-drive System. *J. Elektron. Telekomun.* **2021**, *21*, 79–84. [[CrossRef](#)]
29. Prasanthi, A.; Shareef, H.; Errouissi, R.; Asna, M.; Mohamed, A. Hybridization of battery and ultracapacitor for electric vehicle application with dynamic energy management and non-linear state feedback controller. *Energy Convers. Manag. X* **2022**, *15*, 100266. [[CrossRef](#)]
30. Ahmed, U.O.; Patrick, A.A.; Kwembe, B.A. DC Motor Speed Control using Internal Model Controller Industrial Transformation Strategy. *Int. J. Eng. Adv. Technol.* **2020**, *9*, 300–306. [[CrossRef](#)]
31. Prasanthi, A.; Shareef, H.; Asna, M.; Asrul Ibrahim, A.; Errouissi, R. Optimization of hybrid energy systems and adaptive energy management for hybrid electric vehicles. *Energy Convers. Manag.* **2021**, *243*, 11435. [[CrossRef](#)]
32. Prasanthi, A.; Shareef, H.; Asna, M. Hybrid Energy Storage System Sizing in Electric Vehicles Using Butterfly Optimization Algorithm. In Proceedings of the ZEMCH International Conference, Dubai, United Arab Emirates, 26–28 October 2021; pp. 856–865. Available online: http://www.zemch.org/zemch_conference_proceedings (accessed on 19 April 2023).

Disclaimer/Publisher’s Note: The statements, opinions and data contained in all publications are solely those of the individual author(s) and contributor(s) and not of MDPI and/or the editor(s). MDPI and/or the editor(s) disclaim responsibility for any injury to people or property resulting from any ideas, methods, instructions or products referred to in the content.